Concentration banding instability of a sheared bacterial suspension

Laxminarsimharao Vennamneni[1], Piyush Garg[1] and Ganesh Subramanian[1],†

[1]Engineering Mechanics Unit, JNCASR, Jakkur, Bangalore 560064, India

We demonstrate a novel shear-induced mechanism for growth of concentration fluctuations in a bacterial suspension. Using a linear stability analysis, a homogeneous bacterial suspension, subject to a simple shear flow, is shown to be susceptible to exponentially growing layering perturbations in the shear rate and bacterial concentration. A semi-analytical expression for the growth rate of concentration perturbations is first obtained using the method of multiple scales, in the limit where the time scales characterizing the positional and orientation degrees of freedom are well separated. Next, the eigenspectrum obtained numerically from a full linear stability analysis is used to validate and extend the multiple scales result, and draw a contrast with the known orientation-shear instability. Finally, fully nonlinear simulations, but restricted to one-dimensional variations of the relevant fields (velocity, concentration and swimmer orientation distribution) show that the initial instability leads to gradient-banded velocity profiles, with a local depletion of bacteria at the interface between the homogeneous shear bands. Our results demonstrate that long-ranged hydrodynamic interactions serve as an alternate explanation for recent observations of shear bands in bacterial suspensions.

Key words: micro-organism dynamics, rheology

---

1. Introduction

Long-ranged hydrodynamic interactions in dilute bacterial suspensions drive growing orientation fluctuations, in turn leading to collective motion on length scales much larger than a single bacterium (Koch & Subramanian 2011; Wensink *et al.* 2012; Marchetti *et al.* 2013; Clement *et al.* 2016). While large-scale coherent motion in unsheared bacterial suspensions observed in simulations (Saintillan & Shelley 2007; Underhill, Hernandez-Ortiz & Graham 2008; Krishnamurthy & Subramanian 2015; Stenhammar *et al.* 2017), and in many experiments (Wu & Libchaber 2000; Dombrowski *et al.* 2004; Dunkel *et al.* 2013; Gachelin *et al.* 2014), is regarded as well understood theoretically, much less is known about the dynamics of sheared bacterial suspensions (Clement *et al.* 2016). Several recent experiments have observed counter-intuitive behaviour of bacterial suspensions under an external shear, including regimes of apparent superfluidity (López *et al.* 2015; Guo *et al.* 2018). Here, we demonstrate a novel concentration-shear coupled mechanism for growth of fluctuations in bacterial suspensions, eventually leading to banded steady states. The proposed mechanism is shown to lead to shear bands, with

† Email address for correspondence: sganesh@jncasr.ac.in

concentration inhomogeneities, in the dilute regime itself; in sharp contrast to both passive complex fluids (Cates & Fielding 2006; Olmsted 2008; Divoux *et al.* 2016), and active fluids studied earlier, (Cates *et al.* 2008; Loisy, Eggers & Liverpool 2018) where shear banding is observed/predicted only in the semi-dilute and concentrated regimes.

We first discuss the physical mechanism underlying the proposed instability (illustrated through a schematic in figure 1). In the rest of the paper, the instability is demonstrated through a linear stability analysis, followed by the results of nonlinear simulations. Both the analysis and simulations pertain to a bacterial suspension subjected (on average) to a simple shear flow, and are restricted to perturbations that only vary along the gradient direction of the ambient shear. The bacteria are modelled as slender particles that swim along their axis, while being rotated and aligned by the background shear. The latter leads to a spatially homogeneous sheared suspension with an anisotropic orientation distribution (figure 1*a*). In the dilute regime, the contribution of the anisotropically oriented bacteria to the suspension viscosity is proportional to the local concentration. The flow perturbation created by the tail-actuated swimming mechanism of the oriented bacteria (termed 'pushers') reinforces the fluid flow along the extensional axis of the imposed shear. Hence, the suspension viscosity is reduced below that of the solvent (Hatwalne *et al.* 2004; Sokolov & Aranson 2009; Saintillan 2010; Gachelin *et al.* 2013; López *et al.* 2015; Bechtel & Khair 2017; Nambiar, Nott & Subramanian 2017; Saintillan 2018; Nambiar *et al.* 2019*b*). This is in sharp contrast to suspensions with passive microstructural elements which always resist the imposed shear, leading to an enhanced viscosity (Batchelor 1970). Now, imagine a spontaneous gradient-aligned perturbation that leads to a lower (higher) effective suspension viscosity in regions of higher (lower) concentration (figure 1*b*). The restriction to perturbations varying only along the gradient direction, and the assumed inertialess limit, implies that the shear stress is independent of the gradient coordinate (z). This invariance of the shear stress implies that the higher (lower) concentration layers are subject to a higher (lower) shear rate (figure 1*d*). In the higher shear rate regions, the bacteria are more aligned with the flow and, therefore, have a lower probability of migrating in the gradient direction. In turn, this implies a net drift of bacteria into the higher shear rate (higher concentration) regions. The diffusive motion of bacteria drives an opposing stabilizing flux. The drift overcoming the opposing diffusive flux thus provides a mechanism for exponential growth of gradient-aligned (layering) concentration-shear fluctuations from the homogeneous state (figure 1*c*). Front-actuated swimmers ('pullers') such as algae, and passive rigid rods, increase the suspension viscosity in the dilute regime, leading to a stabilizing drift, and thence, to decaying fluctuations.

Migration of bacteria towards higher-shear rate regions, in inhomogeneous shear flows, leading to so-called shear trapping, has been examined before (Rusconi, Guasto & Stocker 2014; Barry *et al.* 2015; Bearon & Hazel 2015; Ezhilan & Saintillan 2015; Sokolov & Aranson 2016; Vennamneni, Nambiar & Subramanian 2020). However, all of these studies have focused on the kinematic point of view where changes in the bacterial concentration and orientation distribution do not couple back to the flow. The mechanism outlined above illustrates, for the first time, how the back-coupling via the bacterial stress leads to exponentially growing concentration and shear rate fluctuations. Eventually, the growing fluctuations lead to a banded steady state, with homogeneous high-shear bands, containing a marginally higher concentration of bacteria relative to the original base-state, and that are separated by an interface depleted of bacteria.

Gradient banding in sheared active fluids has been so far studied using phenomenological continuum equations which allow for a bulk nematic or polar order. In allowing for such an order, these formulations implicitly assume the orientation degrees of
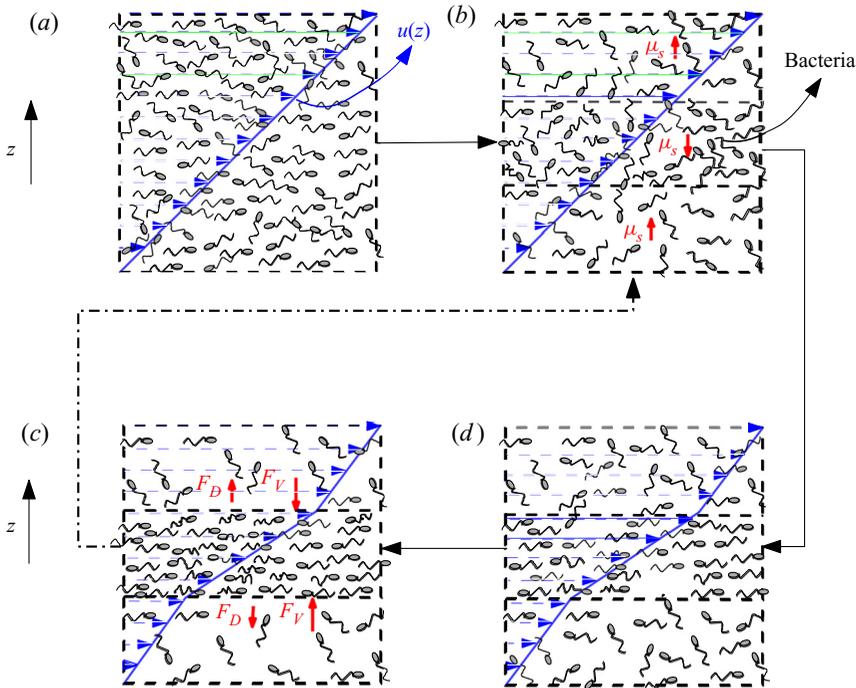
FIGURE 1. Schematic illustrating the physical mechanism of the concentration-banding instability; where μ_s is the suspension viscosity, and F_V and F_D represent the destabilizing and stabilizing fluxes due to drift and diffusion, respectively. (*a*) Homogeneously sheared base-state; (*b*) spontaneous perturbation in the concentration; (*c*) net accumulation in the high shear region and (*d*) induced shear rate perturbation.

freedom to evolve on a slow time scale (Cates *et al.* 2008; Giomi, Liverpool & Marchetti 2010; Fielding, Marenduzzo & Cates 2011; Marchetti *et al.* 2013; Loisy *et al.* 2018). Even in cases where concentration (position) degrees of freedom are incorporated, both the orientation and concentration modes are assumed to evolve on comparably slow time scales (see for instance Giomi, Marchetti & Liverpool 2008). In contrast, in the context of explaining shear-induced migration of bacteria and algae in dilute suspensions (Rusconi *et al.* 2014; Barry *et al.* 2015), it has been shown that the concentration degrees of freedom do evolve on a slower time scale, while the orientation degrees of freedom evolve much faster, and may then be treated in a quasi-steady approximation (Bearon & Hazel 2015; Vennamneni *et al.* 2020). Thus, the phenomenological active fluids approach is not expected to describe shear-induced migration in dilute swimmer suspensions. To the extent that the concentration-shear coupling mechanism described above (figure 1) relies crucially on the shear-induced migration from a lower to a higher concentration layer, the banding instability also lies outside the purview of the aforementioned phenomenological approach. Indeed, earlier results in the literature only report the shear-modified orientation instability leading to collective motion (or bacterial turbulence), already seen in unsheared active fluids (Cates *et al.* 2008; Marchetti *et al.* 2013; Loisy *et al.* 2018). In the specific context of sheared bacterial suspensions, an earlier effort only examined vorticity-aligned perturbations, and therefore did not find the novel concentration-shear instability analysed here (Pahlavan & Saintillan 2011). To the best of our knowledge therefore, this is the first demonstration of a shear-induced mechanism for enhanced fluctuations, leading to gradient banding in an active fluid.

The paper is organized as follows. Section 2 describes the system of equations governing the bacterial suspension. The approach used here is based on the Stokes–Smoluchowski framework, and accordingly, §2.1 briefly discusses the relative merits of the Landau–deGennes (consisting of the phenomenological active-fluid equations mentioned above) and Stokes–Smoluchowski approaches that have most often been used to examine the dynamics of active fluids, including bacterial suspensions. Section 3 outlines the linear stability analyses (§§3.1 and 3.2) and the nonlinear simulations (§3.3). In §3.1, a multiple scale analysis is used to obtain a semi-analytical expression for the growth rate of concentration perturbations in the limit where the time scales for orientation and spatial degrees of freedom are well separated. Next, in §3.2, a full linear stability analysis numerically obtains the growth rate of coupled concentration–orientation perturbations, without any restriction on the underlying time scales. Section 3.3 examines the one-dimensional gradient-banded steady states seen in the nonlinear simulations. In §3.4, we compare our results with a recent experiment studying the rheology of dilute bacterial suspensions (Martinez *et al.* 2020). Finally, in §4, we present the conclusions, while discussing the future scope of this work.

2. Theoretical model

At the microscale, a bacterium swims with a speed U_b, and the swimming direction (p) decorrelates via both rotary diffusion (with diffusivity D_r) and tumbling (at a mean rate τ^{-1}). Using τ and the length (H) and velocity scale (U_∞) of the imposed flow as the time, length and velocity scales, respectively, the non-dimensional kinetic equation for the bacterium phase-space probability density, $\Omega(x, p, t)$ in the dilute limit is given by

$$\frac{\partial \Omega}{\partial t} + (\epsilon p + Pe u) \cdot \nabla_x \Omega - \tau D_r \nabla_p^2 \Omega + Pe \nabla_p \cdot (\dot{p}\Omega) + \left[\Omega - \frac{1}{4\pi} \int dp' \Omega(p')\right] = 0, \tag{2.1}$$

where $\epsilon = U_b \tau / H$ is the ratio of the bacterium run length to the imposed length scale, $Pe = U_\infty \tau / H$ denotes the relative importance of the shear-induced and intrinsic reorientation time scales and τD_r gives the relative importance of tumbling and rotary diffusion. In (2.1), u is the convecting suspension velocity field. Approximating the bacteria as slender force-dipoles, the rotation due to shear flow is given by the Jeffery relation, $\dot{p} = E \cdot p + \omega \cdot p - p(E : pp)$, where E and ω are the strain rate and vorticity tensors, respectively, associated with the local linear flow (Jeffery 1922). As discussed in the introduction, this rotation due to the flow, coupled with swimming, leads to a migration of the bacteria towards the high shear rate regions.

Equation (2.1) is coupled to the inertialess momentum and continuity equations which govern the suspension flow (u), and are given by:

$$\nabla \cdot \Sigma - \nabla P = 0 \implies Pe \nabla^2 u = -\nabla \cdot \Sigma^B + \nabla P, \tag{2.2}$$

$$\nabla \cdot u = 0, \tag{2.3}$$

where P is the suspension pressure and Σ the suspension stress; Σ is a sum of the solvent and active stresses, $\Sigma = \Sigma^B + Pe(\nabla u + \nabla u^T)$, where the stress is scaled by $\mu \tau^{-1}$ with μ being the solvent viscosity. The active stress, Σ^B, is the coarse-grained stress exerted by the particle-phase (bacteria) (Batchelor 1970). We approximate Σ^B by its active contribution alone which, in a continuum framework, is given in terms of the bacterium force-dipole density as $-\mathcal{A} \int dp \Omega(p)(pp - I/3)$. The non-dimensional parameter $\mathcal{A} = \mathcal{C} n_0 L^2 U_b \tau$ is the activity number; here, L is the bacterium length, n_0 the number density and $\mathcal{C}$ the

non-dimensional strength of the intrinsic bacterium force-dipole, with $\mathcal{C} > 0$ for 'pushers' (Koch & Subramanian 2011). The active stress is known to reduce the suspension viscosity (Saintillan 2018), an effect that is crucial to the banding instability analysed here. As will be seen in § 3, the parameters $\mathcal{A}$ and *Pe* delineate the region of instability. In the general case, $\boldsymbol{\Sigma}^B$ has an additional passive stress contribution arising from the bacterium inextensibility. For moderate *Pe*, the regime of interest in this work, the passive stress only acts as an enhanced viscosity. Since this effect has been examined before (Subramanian & Koch 2009), here, we neglect it in order to focus on the active stress and concentration coupling.

2.1. *The Landau–deGennes and the Stokes–Smoluchowski frameworks*

Having summarized the theoretical framework above, it is worth drawing a distinction between the two classes of theoretical models that have been used in the literature to analyse active fluids, bacterial suspensions in particular. The first class of models is based on the phenomenological active-fluid formalism which originated in passive liquid crystal hydrodynamics (De Gennes & Prost 1993). In the original passive version, the equations of motion for the order parameter (nematic or polar orientational order, for instance) were derived based on postulating a free energy functional with the constituent terms postulated based on symmetry arguments. The resulting free energy allows for the onset of bulk orientational order above a threshold volume fraction (under quiescent conditions). This approach has been modified for active fluids with the addition of so-called prohibited terms to the stress and order parameter evolution equations. While the latter addition only serves to renormalize the aforementioned threshold for transition to orientational order, the additional term in the stress leads to a fundamentally new dynamics (Simha & Ramaswamy 2002; Hatwalne *et al.* 2004; Marchetti *et al.* 2013). These equations have since been solved under different circumstances (Cates *et al.* 2008; Giomi *et al.* 2008, 2010; Fielding *et al.* 2011; Loisy *et al.* 2018). The approach has been very successful in explaining a host of novel phenomena across a range of systems all of which come under the general umbrella of active matter (Sanchez *et al.* 2012; Marchetti *et al.* 2013; Doostmohammadi *et al.* 2018); for bacterial suspensions in particular, the results are quite representative at high volume fractions (Wensink *et al.* 2012; Li *et al.* 2019).

In contrast, the second approach, the one adopted in the present manuscript, is suited to dilute suspensions of run-and-tumble and rotary diffusing swimmers (bacteria being a specific example), and thereby, is complementary to the above approach based on the liquid crystal phenomenology. This approach may be termed the Stokes–Smoluchowski framework since, as seen above, the kinetic equation for the bacterial probability density resembles the Smoluchowski equation for Brownian particles (except that the original diffusional relaxation is now complemented by an additional run-and-tumble-driven relaxation). The Smoluchowski equation is coupled to the Stokes equations via the bacterial stress. While restricted in its applicability (to the dilute regime), the model can be derived from first principles, wherein interactions between the bacteria are only retained at a mean-field level (Saintillan & Shelley 2008*a*,*b*; Subramanian & Koch 2009; Koch & Subramanian 2011; Stenhammar *et al.* 2017). As a result the model contains no phenomenological approximations and all the parameters involved can be directly measured in experiments. As already mentioned above, the model has been shown to accurately predict concentration inhomogeneities, resulting from shear-induced migration, in channel flows (Bearon & Hazel 2015; Vennamneni *et al.* 2020).

While the active-fluid formalism has been applied with considerable success to dense active suspensions, its inapplicability in the dilute regime may be seen from the Frank

elastic terms, in the free energy functional, that drive a diffusive relaxation of the order parameter. Such diffusive relaxation may arise from short-range repulsive (excluded volume) interactions between closely spaced bacteria at high volume fractions; there is, however, no notion of such an 'elastic network' formed by bacteria in the dilute regime. Moreover, the diffusive relaxation becomes arbitrarily weak at sufficiently long wavelengths, and as a result, the threshold for the onset of collective motion in a quiescent bacterial suspension, when analysed using the active-fluid formalism, becomes system-size dependent; the threshold scaling as the inverse square of the system size, implying that a bacterial suspension in a large enough domain is always unstable (Simha & Ramaswamy 2002; Marchetti *et al.* 2013). In contrast, the Stokes–Smoluchowski approach leads to a threshold volume fraction that is only a function of the bacterium swimming parameters; in fact, the threshold may be stated in terms of the activity number defined above, and is given by $\mathcal{A}^* = 5(1 + 6\tau D_r)$ (Subramanian & Koch 2009). This threshold has been validated in a recent experiment (Martinez *et al.* 2020), which also discuss the inappropriateness of the aforementioned system-size-dependent threshold. A detailed comparison between the observations of Martinez *et al.* (2020) and results obtained in this paper is carried out in § 3.4. Note that a relaxation driven by Frank elasticity would require redefining the activity number with τ being replaced by L_{sys}^2/D_t, L_{sys} here being the system size and D_t the diffusivity proportional to the Frank elastic constant. The resulting threshold volume fraction may then be written in the form $(n_0 L^3) \sim D_t L/(U L_{sys}^2)$, leading to the inverse-square system-size scaling mentioned above.

To summarize then, the Stokes–Smoluchowski framework used here is appropriate for the dilute bacterial suspensions under consideration; higher volume fractions would necessarily require the phenomenological approach based on the active-fluid formalism above. Use of this latter formalism in the dilute regime can lead to incorrect results since the phenomenological constants involved do not have a direct microscopic interpretation in the dilute limit. To reiterate, in this paper we use the Stokes–Smoluchowski framework which is more appropriate for the aforementioned experiments where novel behaviour is seen at volume fractions as low as 0.75 % (see § 3.4). It should be noted that the kinetic equation (2.1), that lies at the heart of this framework, does not therefore include either direct hydrodynamic or steric interactions between the swimming bacteria. While recent efforts have analysed pairwise hydrodynamic interactions in the Stokes–Smoluchowski framework, this lies beyond the scope of the current effort (Stenhammar *et al.* 2017; Nambiar, Garg & Subramanian 2019*a*).

3. Results and discussion

The homogeneous base-state is given by $\boldsymbol{u}_0 = z\boldsymbol{1}_x$ and an anisotropic orientation distribution $\Omega_0(\boldsymbol{p})$, which needs to be solved for numerically; the numerical method is described in appendix A. Knowing $\Omega_0(\boldsymbol{p})$ allows for the calculation of the stress–shear rate curves for the homogeneous state. Figures 2(*a*) and 2(*b*) show the variation of the suspension shear stress (Σ_0) and the suspension viscosity (μ_{s0}) with *Pe*, respectively. For $\mathcal{A} < \mathcal{A}^*$, the suspension shear stress in the base-state (Σ_0) is a monotonically increasing function of the shear rate although the effective viscosity is lower than the solvent viscosity; $\mathcal{A}^* \approx 35$ marks the threshold for the instability in an unsheared suspension owing to the viscosity vanishing at $Pe = 0$ (Subramanian & Koch 2009). For $\mathcal{A} > \mathcal{A}^*$, Σ_0 is a non-monotonic function of *Pe* and the suspension has a zero viscosity at $Pe \equiv Pe_{cr}(\mathcal{A})$; Pe_{cr} being an increasing function of $\mathcal{A}$, with $Pe_{cr}(\mathcal{A}^*) = 0$. We examine the stability of this homogeneous state to gradient-aligned perturbations in the velocity field (u_1) and orientation distribution (Ω_1). Since gradient-aligned perturbations are the long-time
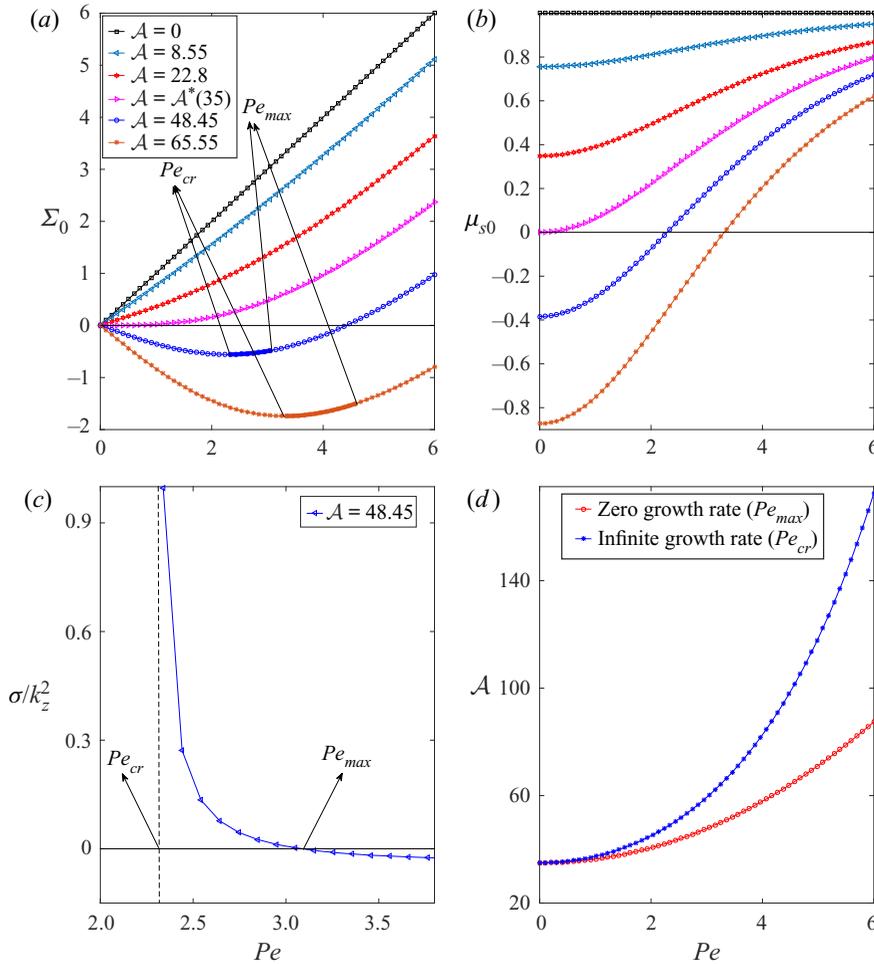
FIGURE 2. A sheared bacterial suspension with $\tau D_r = 1$. (a) The variation of the homogeneous base-state stress with Pe. (b) The variation of suspension viscosity with Pe. (c) The growth rate of layering perturbations, predicted by the multiple scale analysis, versus Pe. (d) The unstable interval of Pe values, corresponding to the concentration-shear instability, in the $\mathcal{A}$–Pe plane. The Pe values marking the endpoints of the unstable interval are Pe_{cr} (corresponding to an infinite growth rate) and Pe_{max} (corresponding to a zero growth rate); the Pe_{cr} and Pe_{max} values are also marked in (a).

limit for almost any initial wavevector in simple shear flow, the assumption of gradient alignment is not restrictive.

In what follows, we examine the linear stability of gradient-aligned concentration perturbations alone in § 3.1 via a multiple scale analysis, the linear stability of all gradient-aligned perturbations in § 3.2 and finally, the fully nonlinear evolution of such perturbations in § 3.3. The bacterial suspension is assumed to be unbounded in extent in all of the above. Confinement of swimmer suspensions is known to lead to concentration inhomogeneities via wall accumulation of swimming bacteria through both kinematic and hydrodynamic mechanisms (Berke *et al.* 2008; Drescher *et al.* 2011; Elgeti & Gompper 2016). However, in order to focus on concentration inhomogeneities arising from banding

in the bulk, we neglect wall effects in the analysis, and impose periodic boundary conditions in the gradient direction in both the stability analysis and the simulations.

3.1. *Concentration dynamics (CD)*

In the limit $\epsilon = U_b\tau/H \to 0$, concentration fluctuations ($n_1 = \int \Omega_1 \, d\boldsymbol{p}$) evolve on a slower, diffusive, time scale ($t_2 \sim O(H^2/(\tau U_b^2))$) compared to orientation fluctuations ($t_1 \sim O(\tau)$). Using a multiple time scale formalism, Ω_1 may, in this limit, be expanded as

$$\Omega_1 = \Omega_{10}(\boldsymbol{p}, t_1)n_1(z, t_2) + \epsilon\Omega_{11}(\boldsymbol{p}, t_1) + \epsilon^2\Omega_{12}(\boldsymbol{p}, t_1). \tag{3.1}$$

The orientation degrees of freedom evolve quasi-statically on the time scales of interest ($t_2/t_1 \sim O(1/\epsilon^2) \gg 1$), and a reduced equation governing n_1 can be derived as (see appendix B.1; Subramanian & Brady 2004; Kasyap & Koch 2014; Vennamneni *et al.* 2020)

$$\frac{\partial n_1}{\partial t_2} = \frac{\partial}{\partial z}\left(-V_1 + D_0\frac{\partial n_1}{\partial z}\right). \tag{3.2}$$

The concentration perturbations (n_1) are thus governed by a drift-diffusion equation. The combination of swimming and orientation decorrelation results in the swimmers undergoing a diffusive motion for long times, with an effective diffusivity D_0, in (3.2). In the absence of flow, the effective diffusivity can be analytically obtained as $D_0 = 1/(3(1 + 2\tau D_r))$ (see, for instance, Krishnamurthy & Subramanian 2015). In the presence of flow, the effective diffusivity also depends on the Péclet number and needs to be calculated numerically; the procedure is outlined in appendix B.1. The differential rotation due to the inhomogeneous perturbed shear flow leads to the additional drift term, V_1, in (3.2). As shown in appendix B.1, the drift term is proportional to the perturbation shear rate gradient and given by,

$$V_1 = 2\sqrt{\frac{\pi}{3}}e_{1,0}\frac{\partial\dot{\gamma}_1}{\partial z}, \tag{3.3}$$

where $e_{1,0}$ is representative of the magnitude of the drift. $e_{1,0}$ is a function of τD_r and Pe and is obtained numerically (see appendix B.1). We find that $e_{1,0} > 0$ and thus the drift is directed from low to high shear rate regions. As explained in the introduction, the sign of the drift is rationalized by noting that swimmers in the high shear rate regions are more aligned with the flow and hence have a lesser probability of migrating in the gradient direction when compared to swimmers in the low shear rate regions. Hence, the drift drives a destabilizing flux from regions of low to high shear rate (figure 1). The diffusive contribution ($D_0 > 0$) (the second term in (3.2)), on the other hand, drives an opposing flux that is stabilizing.

The perturbation shear rate ($\dot{\gamma}_1$) in (3.3) is obtained from the momentum equation as

$$(Pe\mu_{s0})\frac{\partial\dot{\gamma}_1}{\partial z} = \frac{\partial n_1}{\partial z}|\Sigma_0^B|, \tag{3.4}$$

where μ_{s0} is the suspension viscosity and Σ_0^B the active shear stress in the homogeneous state; the respective expressions are given in appendix B.1. Assuming normal modes of the form $[n_1, \dot{\gamma}_1] = [\tilde{n}_1, \tilde{\dot{\gamma}}_1]\cos(zk_z)\exp(\sigma t_2)$, we obtain the following semi-analytical

expression for the eigenvalue governing the evolution of concentration perturbations

$$\sigma = k_z^2 \left(2\sqrt{\frac{\pi}{3}} e_{1,0} \frac{|\Sigma_0^B|}{Pe\mu_{s0}} - D_0 \right). \tag{3.5}$$

When the first term in (3.5), denoting the destabilizing drift, exceeds the diffusivity, $\sigma > 0$, and the homogeneous state becomes unstable (figure 2c). For $Pe \to Pe_{cr}$, the suspension viscosity (μ_{s0}) vanishes and the destabilizing drift diverges in (3.5), making the suspension infinitely susceptible to growing concentration fluctuations (figure 2c). The lower (Pe_{cr}) and upper (Pe_{max}) Péclet thresholds for the concentration-shear instability as a function of $\mathcal{A}$ are shown in figure 2(d), with the range of (dimensionless) unstable shear rates (Pe_{cr}, Pe_{max}) increasing with increasing $\mathcal{A}$.

3.2. *Coupled concentration and orientation dynamics (CCOD)*

The divergence of the growth rate for $Pe \to Pe_{cr}^+$, seen in figure 2(c), is an artefact of the multiple scale analysis. As Pe approaches Pe_{cr}, the time scale (defined as the inverse of the growth rate) characterizing the concentration perturbations decreases, until for Pe sufficiently close to Pe_{cr}, the growth rate $\sigma \sim \tau^{-1}$, or alternatively, the wavenumber in the gradient direction, $k_z \sim (U_b\tau)^{-1}$, and the assumed separation of scales between the concentration and orientation fluctuations is no longer present. The predictions of the multiple scale analysis are thus invalidated for Pe sufficiently close to Pe_{cr}. In order to analyse the behaviour of perturbations across $Pe = Pe_{cr}$, we therefore carry out a linear stability analysis without the assumption of a time scale separation. The complete eigenspectrum, corresponding to any small-amplitude perturbation aligned along the gradient direction, is obtained numerically by expanding the relevant fields in spherical harmonics. The details of the numerical method are given in appendix B.2.

Figure 3 (inset) shows good agreement between the two approaches (the multiple scale and the full linear stability analyses) for $Pe > Pe_{cr}$. Importantly, the full analysis continues to predict a finite growth rate of $O(1/\tau)$ for $Pe \to Pe_{cr}$. The multiple scale analysis also does not predict a finite length scale for the fastest growing mode since $\sigma \propto k_z^2$ (see (3.5)), so that the shortest-wavelength modes are predicted to grow at the fastest rates. In contrast, the full stability analysis, with the orientation dynamics included, predicts the fastest growing wavenumber to be $O(1/(U_b\tau))$ such that the relaxation times of the concentration and orientation (and thence, stress) fluctuations become comparable, both being $O(\tau)$ (see figure 4a). For $k_z > O(1/(U_b\tau))$, the diffusive rate of accumulation of bacteria ($k_z^{-2}/(\tau U_b^2)$) would exceed the stress relaxation time (τ), and hence, such perturbations decay.

The full analysis also predicts the orientation-shear instability, which has earlier been interpreted as a negative-viscosity instability responsible for the onset of collective motion (bacterial turbulence) in a quiescent bacterial suspension. The orientation-shear instability has been studied earlier in the absence of an imposed shear ($Pe = 0$). It is a long-wavelength instability, with $k_z = 0$ being the most unstable mode, and having a finite growth rate. The longest-wavelength perturbations may be regarded as homogeneous shearing flows, on the scale of the bacterium swimming motion, and the response to this homogeneous shear may then be interpreted in terms of the aforementioned negative viscosity (see discussion in § 3.1 of Subramanian & Koch 2009). Importantly, the unstable eigenfunction is spatially homogeneous, implying that concentration fluctuations are absent at the onset of the orientation-shear instability (Underhill *et al.* 2008;
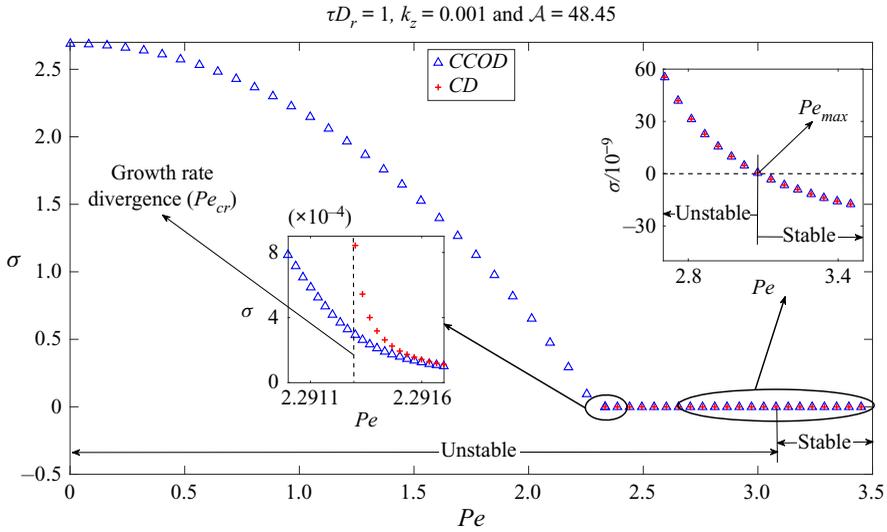
$\tau D_r = 1$, $k_z = 0.001$ and $\mathcal{A} = 48.45$

FIGURE 3. Comparison of growth rates versus *Pe* obtained from the concentration dynamics (§ 3.1) and coupled concentration–orientation dynamics (§ 3.2) analyses. The magnified inset emphasizes the agreement between the two approaches for $Pe > Pe_{cr}$.
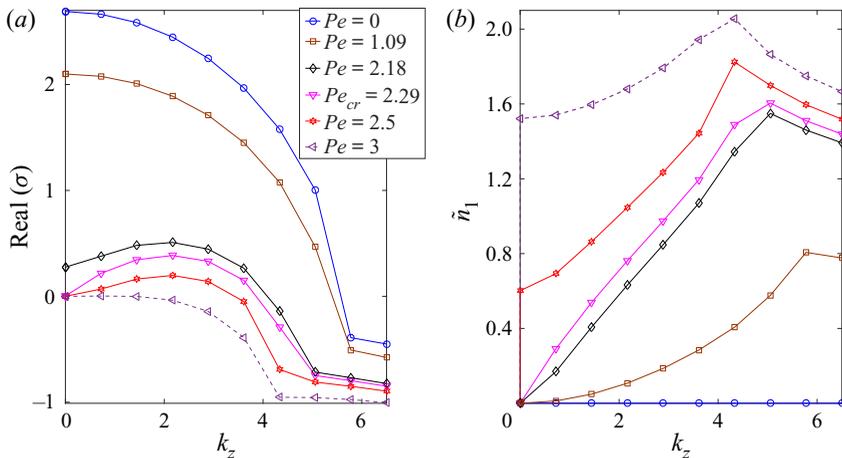

FIGURE 4. Variation in the (*a*) growth rate and (*b*) the amplitude of concentration fluctuations ($\tilde{n}_1$) as a function of the wavenumber for different *Pe* with $\tau D_r = 1$, $\mathcal{A} = 48.5$ ($Pe_{cr} \approx 2.29$ and $Pe_{max} \approx 3.1$). Here, the growth rate (σ) and the wavenumber (k_z) are non-dimensionalized using the bacterium tumble time τ and run length $U_b\tau$, respectively.

Subramanian & Koch 2009). These features are in contrast with the concentration-shear instability described here.

In light of the aforementioned discussion, one thus needs to distinguish between the orientation-shear and concentration-shear instability mechanisms which operate in distinct parameter regimes. The instability onset, regardless of the mechanism, coincides with the stress becoming a non-monotonic function of the shear rate – this corresponds to the curves for $\mathcal{A} > \mathcal{A}^*$ in figure 2(*a*). For $\mathcal{A} > \mathcal{A}^*$, figure 3 shows that orientation

fluctuations drive an instability on the negative-viscosity portion of the stress–shear rate curve corresponding to $Pe < Pe_{cr}$, with this orientation-shear instability arising due to a negative apparent viscosity, as mentioned above, and being the equivalent of the mechanical shear-banding instability known from earlier investigations of passive complex fluids (Cates & Fielding 2006); the novel concentration-shear instability exists only on the positive-viscosity branch of the stress–shear curve corresponding to $Pe_{cr} < Pe < Pe_{max}$.

The two instabilities are most easily be differentiated by focusing on the behaviour of the spatially homogeneous ($k_z = 0$) mode since it corresponds to pure orientation fluctuations without associated concentration fluctuations. For the orientation-shear instability at $Pe = 0$ the most unstable eigenfunction is known to be spatially homogeneous (with $k_z = 0$) from earlier work (Underhill *et al.* 2008; Subramanian & Koch 2009). Figure 4(*a*) shows that the $k_z = 0$ mode remains the fastest growing perturbation in the presence of a weak shear ('weak' here corresponding to the interval $Pe < Pe_{cr}$), and hence the growth may be regarded as being due to a mechanism analogous to the original orientation-shear instability. As argued in Subramanian & Koch (2009), the growth arises because bacteria orient, in response to a long-wavelength perturbation, so that the resulting bacterium flow fields reinforce the original perturbation; as stated above, this reinforcing mechanism may be interpreted in terms of a negative viscosity. In stark contrast, figure 4(*a*) shows that for $Pe > Pe_{cr}$, the $k_z = 0$ mode is stable and the most unstable eigenfunction now has a spatially modulated structure (a finite k_z) corresponding to a layering perturbation. Thus, in the interval $Pe_{cr} < Pe < Pe_{max}$, the mechanism underlying the growth involves the concentration-shear coupling discussed earlier. For Pe in the neighbourhood of Pe_{cr}, there is no sharp distinction between the two instability mechanisms.

Further insight into the distinction between the two instability mechanisms may be obtained from the behaviour of the long-wavelength number density perturbations ($\tilde{n}_1$) shown in figure 4(*b*). In an unsheared suspension, the unstable eigenfunction does not have number density perturbations for any k_z (the curve in figure 4(*b*) for $Pe = 0$) in agreement with earlier predictions (Underhill *et al.* 2008; Subramanian & Koch 2009). Figure 4(*b*) shows that weak shear only leads to weak long-wavelength number density perturbations ($\tilde{n}_1 \to 0$ as $k_z \to 0$) for $Pe < Pe_{cr}$. However, the behaviour of these number density perturbations is significantly altered for $Pe > Pe_{cr}$. For $Pe > Pe_{cr}$, there are strong, long-wavelength concentration fluctuations as predicted by the mechanism outlined earlier. This is seen in figure 4(*b*) where the amplitude of these fluctuations $\tilde{n}_1$ now approaches a finite value even as $k_z \to 0$ (with $\tilde{n}_1 = 0$ for $k_z = 0$ being a singular limit). Along with the results of the multiple scale analysis in § 3.1, this clearly shows that it is the concentration-shear coupling mechanism that leads to an instability for $Pe > Pe_{cr}$.

3.3. *Nonlinear simulations*

To examine the steady state resulting from the linear instability discussed above, we numerically integrate (2.1) and (2.3) in time. The nonlinear simulations are carried out in two dimensions, so the orientation vector is restricted to the unit circle, and may be characterized by a single azimuthal angle. A standard spectral formulation is used for the simulations and the details are given in appendix C. The simulation results are validated by comparing against the linear stability analysis during the initial phase of exponential growth (see appendix C). The imposed non-dimensional shear rate (Pe) is taken to be the control parameter.

Figure 5(*a*–*c*) shows the evolution of the velocity, shear rate and concentration fields over time for $Pe = 0.75$ and $\mathcal{A} = 62.83$ with $\tau D_r = 0.0025$. For this choice of parameters, $Pe_{cr} \approx 0.67$ and $Pe_{max} \approx 0.975$, so that the chosen Pe lies in the concentration-shear
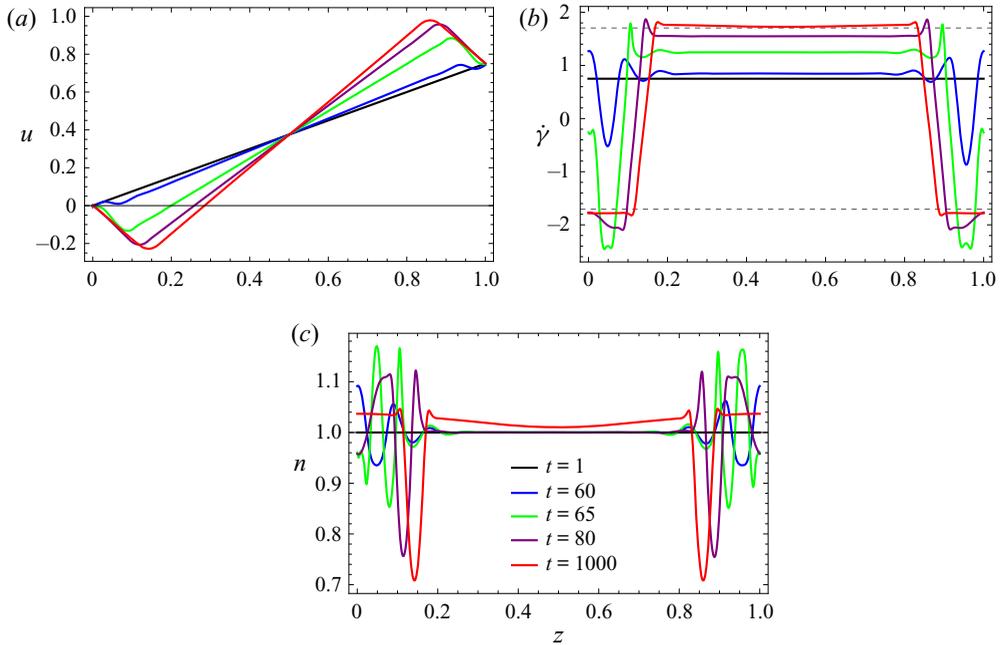
FIGURE 5. The time evolution of (a) the velocity (u), (b) shear rate ($\dot{\gamma}$) and (c) concentration (n) fields towards the gradient banded steady state for $Pe = 0.75$. The simulations have a box size 10 times the run length $U_b\tau$ with $\tau D_r = 0.0025$ and $\mathcal{A} = 62.83$; for these parameters, $Pe_{cr} \approx 0.67$ and $Pe_{max} \approx 0.975$. The shear rates $\dot{\gamma}^\star$ and $-\dot{\gamma}^\star$ are also marked as dashed lines in (b).

instability regime. The chosen initial condition is given in appendix C. The velocity field evolves from the initial near-homogeneous shear to a banded steady state, with equal and opposite shear rates in two (unequal) bands, for long times. From figure 5(b), the shear rates selected in the bands are seen to be $\dot{\gamma}^\star \approx 1.69$ and $-\dot{\gamma}^\star$. The associated concentration field shows that the two shear bands are homogeneous at steady state, with a localized depletion of bacteria only at the interface between the bands (see figure 5c), this depletion being consistent with earlier findings of high-shear trapping in inhomogeneous shearing flows (Rusconi *et al.* 2014; Bearon & Hazel 2015; Vennamneni *et al.* 2020). Note that, despite the appearance, there are only two bands (and one shear interface) at steady state, and not three, since the profiles may be shifted by an arbitrary amount in the gradient direction on account of the periodic boundary conditions. Figure 6 shows the time evolution of the associated suspension stress for different Pe, including the case $Pe = 0.75$ examined in figure 5. For all cases, the suspension stress asymptotes to zero for long times. Figure 7(a–c) shows the steady-state velocity, shear rate and concentration fields for varying Pe. Thus, for all Pe examined, a gradient-banded state results for long times; two bands with differing shear rates coexist at the same (zero) shear stress. The selected shear rate in the bands is seen to be independent of Pe. In light of figure 6, the only criterion controlling the shear rate selected at steady state is that of the shear stress being zero. As a result, the only consequence of varying the imposed shear rate is to alter the relative widths of the two shear bands in a manner so as to accommodate the imposed shear. For $Pe = 0$ alone, the two bands have equal thicknesses, each occupying half the simulation domain.
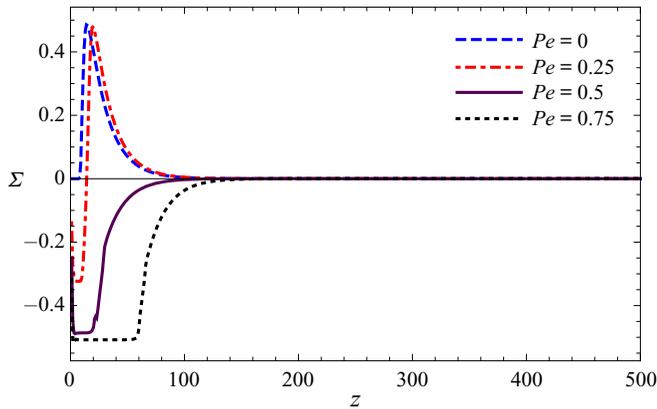
FIGURE 6. The time evolution of the suspension shear stress (Σ) for various Pe. The simulations have a box size 10 times the run length $U_b\tau$ with $\tau D_r = 0.0025$ and $\mathcal{A} = 62.83$; for these parameters, $Pe_{cr} \approx 0.67$ and $Pe_{max} \approx 0.975$.

FIGURE 7. (*a*) The velocity (u), (*b*) the shear rate ($\dot{\gamma}$) and (*c*) the concentration (n) profiles in the nonlinear banded state. The simulations have a box size 10 times the run length $U_b\tau$ with $\tau D_r = 0.0025$ and $\mathcal{A} = 62.83$; for these para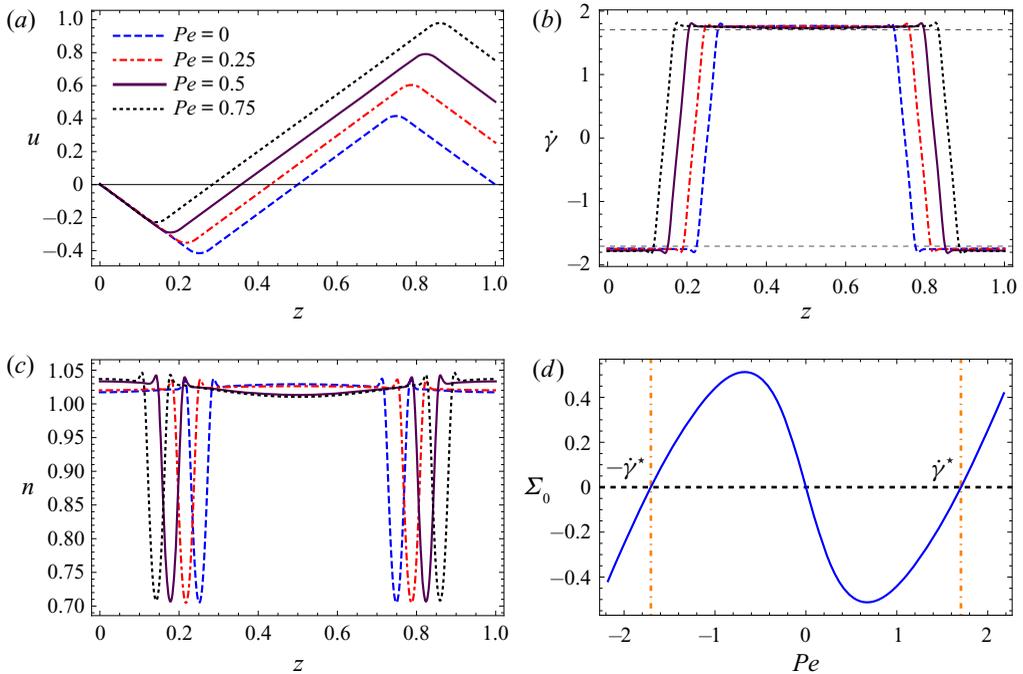meters, $Pe_{cr} \approx 0.67$ and $Pe_{max} \approx 0.975$. (*d*) Maxwell construction showing selected the shear rate ($\dot{\gamma}^\star \approx 1.69$), with zero stress, selected in the banded state. The shear rates $\dot{\gamma}^\star$ and $-\dot{\gamma}^\star$ are also marked as dashed lines in (*b*).

Further, the steady-state banded profiles do no show any major difference across $Pe_{cr} (\approx 0.67$ in figure 7) even though concentration fluctuations are crucial for the instability, and therefore, the start-up kinetics for $Pe > Pe_{cr}$. We thus see that both the orientation-shear and concentration-shear instabilities, unexpectedly, lead to a similar nonlinear gradient

banded state. This insensitivity of the selected stress to concentration coupling is in contrast to shear banding in passive complex fluids, where this coupling leads to an increase in the selected stress with the shear rate (Fielding & Olmsted 2003; Cates & Fielding 2006).

Having characterized the nature of the inhomogeneous (gradient-banded) steady state, we now show that a geometric construction based on the homogeneous stress–shear rate curve can be used to predict the selected stress and shear rates in this banded state. Figure 7(*d*) shows the homogeneous stress–shear curve from figure 2(*a*) together with its (symmetric) extension to negative shear rates. If we assume a homogeneous concentration profile in the banded state, then knowing the magnitude (zero) of the shear stress from figure 6, we can find the corresponding selected shear rates from figure 7(*d*). The selected shear rates are seen to be $\dot{\gamma}^{\star}$ and $-\dot{\gamma}^{\star}$. Figure 7(*d*) thus suggests a banded state with equal and opposite shear rates $\dot{\gamma}^{\star}$ which supports a zero bulk stress with a homogeneous concentration. Rather remarkably, the shear rate and stress in the banded state closely follow the geometric construction, even though the concentration profile is not completely homogeneous. This construction is seen to be the equivalent of the Maxwell construction used in equilibrium thermodynamics, with the shear rate playing the role of the specific volume in the familiar one-component system. However, unlike equilibrium thermodynamics, the geometric construction cannot be used to predict the shear stress in the banded state (Cates & Fielding 2006; Dhont & Briels 2008; Olmsted 2008).

The equal and oppositely sheared zones in the banded state imply that the shear rate goes through zero at the interface, driving a local depletion of bacteria (Vennamneni *et al.* 2020) as seen in figure 7(*c*). The Maxwell construction in figure 7(*d*) is relevant for an infinitely large system in the gradient direction; however, figure 7(*c*) shows that the bands in a finite system have a marginally higher concentration of bacteria than the original homogeneous state state due to interfacial depletion. Thus, the selected shear rate slightly differs from $\dot{\gamma}^{\star}$, the value suggested by the Maxwell construction in figure 7(*d*). This in turn implies that the stress selected is finite, but (very) small in magnitude. The width of the interface between the shear bands is of the order of the bacterium run length ($U_b\tau$), which can be seen from (2.1) to be the length scale governing the spatial decay of stress. With increasing box size, the extent of the interfacial depletion reduces, and the shear rate selected approaches $\dot{\gamma}^{\star}$ predicted by the Maxwell construction (not shown).

An analogous result for the selected stress was obtained earlier for extensile active nematics for nematic–nematic banding and no concentration variation (Cates *et al.* 2008; Fielding *et al.* 2011). In this approach, the shear rate is exactly the prediction of the Maxwell construction, since there is no concentration variable (Cates *et al.* 2008). As discussed in § 2.1, the active–nematic formalism, however, has phenomenological constants that do not have a direct microscopic interpretation, and as pointed our earlier, is not expected to work for dilute bacterial suspensions that are far from an isotropic–nematic transition. This is evident from Giomi *et al.* (2010) and Loisy *et al.* (2018) reporting similar stress–shear rate curves and yet very different velocity profiles from those in Cates *et al.* (2008) and Fielding *et al.* (2011). In contrast, our approach solves the underlying kinetic equation directly and rigorously demonstrates the selection of a banded state even in the dilute regime. Crucially, our results demonstrate that long-range hydrodynamic interactions offer an alternate explanation for experimental observations of a banded state in dilute bacterial suspensions (Martinez *et al.* 2020). A more detailed comparison with recent experimental results follows.

3.4. *Comparison with Martinez et al. (2020)*

Martinez *et al.* (2020) have recently studied the rheology of bacterial suspensions by measuring both the viscosity and the velocity profile of a sheared suspension of *Escherichia coli* using a Couette and cone-plate rheometer, respectively. This dual measurement allows the authors, for the first time, to ascertain the role of collective motion on the measured rheology. The authors examine a range of (small) volume fractions both in the absence and presence of collective motion. At volume fractions less than 0.75 %, with an imposed shear rate of 0.04 s^{-1} (corresponding to the linear response regime with $Pe = \dot{\gamma}\tau \ll 1$), they observe that the zero-shear viscosity decreases with increasing volume fraction. The authors verified the absence of collective motion at these volume fractions based on the velocity profile in the cone-plate rheometer being a simple shear. This decrease in the viscosity, in the absence of collective motion, has been explained based on both the Stokes–Smoluchowski (Bechtel & Khair 2017; Nambiar *et al.* 2017) and Landau–deGennes (Hatwalne *et al.* 2004; Cates *et al.* 2008) frameworks, with the viscosity reduction being dependent on the system size in the latter case. To compare the two predictions, the authors carried out viscosity measurements for different gap sizes in the Couette rheometer. They did not observe any system size dependence, and therefore conclude that the Stokes–Smoluchowski framework is appropriate for explaining the experimental results at the low volume fractions under consideration.

Furthermore, Martinez *et al.* (2020) are also the first to report the existence of an intrinsic threshold volume fraction for the onset of collective motion. There have been earlier reports of a threshold volume fraction for the onset of collective motion in bacterial suspensions conforming to a thin-film geometry (Sokolov *et al.* 2007; Sokolov & Aranson 2012). However, the thickness of the film was not varied systematically in these experiments, and thus there was no way of inferring system-size dependence. In contrast, Martinez *et al.* (2020) systematically vary the gap size of the Couette rheometer to establish that the threshold volume fraction is indeed independent of the confining system size. As seen in § 2.1, the existence of a system-size independent threshold is one of the central predictions of the Stokes–Smoluchowski framework, and it is therefore of interest to compare the experimental and theoretical thresholds (Subramanian & Koch 2009). Martinez *et al.* (2020) report the onset of collective motion for volume fractions greater than 0.75 %, the threshold being valid both in the absence of an external flow as well as at a low shear rate of 0.04 s^{-1} (used for the aforementioned viscosity measurements). The volume fraction (0.75 %) in the experiments was calculated using the cell body volume and corresponds to a hydrodynamic volume fraction (n_0L^3) of around 5.25 by assuming an estimate for the bacterium length (L) of 10 μm (Linek *et al.* 2016). Recall from § 2 that the theoretical model predicts the onset in terms of the non-dimensional activity number, $\mathcal{A} = \mathcal{C}n_0L^2U_b\tau$. The hydrodynamic volume fraction (n_0L^3) is the relevant parameter for slender particles, and the threshold hydrodynamic volume fraction is then given as $(n_0L^3)_c = (\mathcal{A}^*/\mathcal{C})(L/U_b\tau)$. For the *E. coli* strain used by the authors, the parameters have been estimated as $L = 10$ μm, $U_b = 10$ μm s^{-1}, $\tau = 1$ s and $\tau D_r = 0$ (Linek *et al.* 2016); $\tau D_r = 0$ is consistent with Martinez *et al.* (2020) restricting themselves to the pure run-and-tumble case. Using $\mathcal{A}^* \sim 5$ for the low *Pe* numbers accessed in the experiment, we thus get $n_0L^3 = 5/\mathcal{C}$, where $\mathcal{C}$ is the strength of the dipole constant. The dipole constant has not been experimentally determined, but is expected to be $O(1)$ for typical swimmers, since it is defined by requiring the dimensional force dipole to be μUL^2. Thus, for $O(1)$ values of $\mathcal{C}$, the experimental and theoretical thresholds are indeed in agreement. It should be noted that work on passive fibre suspensions has shown that the dilute Stokes–Smoluchowski framework is applicable up to hydrodynamic volume

fractions of around 10 (see for instance chapter 10 in Larson (2013) and Mackaplow & Shaqfeh (1998)), and hence the observed threshold lies within the validity of the dilute theory.

Martinez *et al.* (2020) also show that the suspension viscosity becomes nearly zero and approximately invariant with the volume fraction for volume fractions greater than 0.75% (see figure 4*a* in Martinez *et al.* 2020). Further the velocity profile is no longer simple shear flow. Instead, shear banding is observed such that bands with multiple shear rates are observed at the same shear stress (see figure 4*b*–*g* in Martinez *et al.* 2020). Recall from § 3.3 that upon the onset of the orientation-shear instability the theoretical model also predicts shear bands (see figure 7*a*) and a zero viscosity independent of the volume fraction. Thus, we see that the experimental and simulation results are in qualitative agreement even with the simplifying assumption of only gradient direction variations made in the simulations. Guo *et al.* (2018) have also reported shear banding in bacterial suspensions at moderate volume fractions recently. However, these experiments were conducted in a highly confined setting with a gap width of 60 μm, and swimmer interactions with boundaries are expected to play a dominant role. Note that, in the experiments of Martinez *et al.* (2020) above, the threshold was found to approach the prediction of the unbounded-domain theory only for gap sizes larger than 200 μm. Since we ignore the effects of confinement, our results cannot be directly applied to Guo *et al.* (2018), and can at best serve as a qualitative explanation.

To summarize, we see that the Stokes–Smoluchowski framework used in this paper accurately predicts the threshold for the onset of collective motion observed in recent experiments. The same framework also qualitatively predicts the viscosity and the velocity profiles observed beyond the threshold. Recent work has already shown that this framework accurately describes the rheological properties of bacterial suspensions in the absence of collective motion (Bechtel & Khair 2017; Saintillan 2018; Nambiar *et al.* 2019*b*; Martinez *et al.* 2020). Complementing these efforts, our work thus establishes that the Stokes–Smoluchowski framework is appropriate for the examination of the rheological properties of dilute bacterial suspensions across the collective motion threshold.

4. Concluding remarks

We have demonstrated a novel concentration-shear instability mechanism in dilute bacterial suspensions. The proposed instability is reminiscent of the Helfand–Federickson mechanism that explains shear-enhanced concentration fluctuations in concentrated polymer solutions near an equilibrium critical point (Helfand & Fredrickson 1989; Wu, Pine & Dixon 1991; Dixon, Pine & Wu 1992; Larson 1992; Milner 1993; Onuki 2002; Fielding & Olmsted 2003; Cromer *et al.* 2013; Cromer, Fredrickson & Leal 2014). However, dilute bacterial suspensions are far from any critical point and the dynamics of the enhanced concentration fluctuations is crucially reliant on the novel rheological response arising from bacterial activity. We hope that the theoretical results reported here would motivate light scattering experiments examining the dynamics of concentration fluctuations in bacterial suspensions. Similar experiments in polymer solutions have shed considerable light on the nature of the shear-enhanced concentration fluctuations (Wu *et al.* 1991; Dixon *et al.* 1992).

The concentration-shear instability mechanism need not be restricted to a rheological scenario. Observations of collective motion driven by concentration fluctuations near the contact line of an evaporating drop were reported in Kasyap, Koch & Wu (2014), and in pressure-driven pipe flow in Secchi *et al.* (2016). The generalization of our results to an inhomogeneous shear flow would lead to additional insight into these observations.

Although for the imposed linear flow considered here, the concentration fluctuations have been found to vanish in the bulk at steady state, one nevertheless expects them to play a key role in a general non-stationary scenario. Even at steady state, the localized depletion in bacterial concentration at the interface between the homogeneous shear bands, and the resulting localization in the stress, is expected to render the banded-state susceptible to secondary interfacial instabilities (Fielding 2005; Miles *et al.* 2019).

Finally, the unique ability of shear to enhance concentration fluctuations in active suspensions need not be limited to pushers. The recent identification (Barry *et al.* 2015), and subsequent explanation (Vennamneni *et al.* 2020) of a low-shear trapping regime, implies that an imposed shear may also be capable of enhancing concentration fluctuations in suspensions of pullers (algae with contractile force dipoles, for instance). The role of concentration fluctuations is expected to be substantial in this case owing to the phenomenon of centreline collapse that has been predicted to occur above a critical swimmer aspect ratio (Vennamneni *et al.* 2020).

Acknowledgements

Declaration of interests

The authors report no conflict of interest.

Appendix A. The base-state

The bacterium orientation, in the chosen spherical coordinate system, is depicted in figure 8. In the base-state, whose stability we examine in the paper, the bacteria are homogeneously distributed in the gradient direction and have an anisotropic orientation distribution due to rotation by the imposed shear flow. The resulting homogeneous active stress does not induce any fluid flow, and thus the flow field remains identical to the imposed shear, $u_0 = z\mathbf{1}_x$. The momentum and continuity equations (2.3) are, thus, trivially satisfied. From (2.1), the equation governing the orientation distribution (Ω_0) is

$$Pe\nabla_p \cdot (\dot{p}'\Omega_0) + \left[\Omega_0 - \int \mathrm{d}p' \frac{1}{4\pi}\Omega_0(p')\right] - D_r\tau\nabla_p^2\Omega_0 = 0. \qquad (A\,1)$$

A.1. *Numerical solution of the base-state probability density*

Here we describe the numerical scheme for solving (A 1) for the base-state probability density (Ω_0), and hence, the base-state stress Σ_0 (Nambiar *et al.* 2017, 2019*b*; Vennamneni *et al.* 2020). Considering $\nabla_p \cdot (\dot{p}'\Omega_0)$, the first term in (A 1), substituting $\dot{p}'$, and after simplification, one may write

$$\nabla_p \cdot (\dot{p}'\Omega_0(p)) = \cos^2\theta\cos\phi\frac{\partial\Omega_0}{\partial\theta} - \cot\theta\sin\phi\frac{\partial\Omega_0}{\partial\phi} - 3\Omega_0\sin\theta\cos\theta\cos\phi$$

$$= \mathrm{i}\cos^2\theta\mathcal{L}_y(\Omega_0) - \mathrm{i}\sin\theta\cos\theta\sin\phi\mathcal{L}_z(\Omega_0) - 3\sin\theta\cos\theta\cos\phi\Omega_0,$$
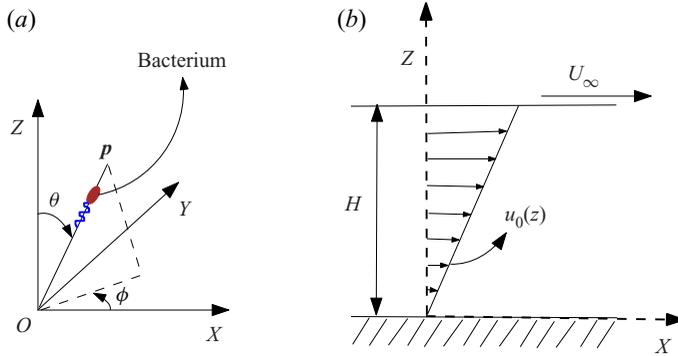$$(A\,2)$$

FIGURE 8. Schematic showing the (*a*) coordinate system for a bacterium with orientation $\boldsymbol{p}$ (*b*) a bacterial suspension subjected to simple shear flow.

where the operators

$$\mathcal{L}_y = -\mathrm{i}\cos\phi\frac{\partial}{\partial\theta} + \mathrm{i}\cot\theta\sin\phi\frac{\partial}{\partial\phi}, \tag{A 3}$$

$$\mathcal{L}_z = -\mathrm{i}\frac{\partial}{\partial\phi}. \tag{A 4}$$

Now, rewriting (A 2) with the coefficients of partial derivatives written in terms of spherical harmonics

$$\nabla_p \cdot (\dot{\boldsymbol{p}}'\Omega_0(\boldsymbol{p})) = \left(\frac{2}{3}\sqrt{\frac{4\pi}{5}}Y_2^0 + \frac{1}{3}\sqrt{4\pi}Y_0^0\right)\mathrm{i}\mathcal{L}_y(\Omega_0) + \sqrt{\frac{2\pi}{15}}\left(Y_2^{-1} + Y_2^1\right)\mathcal{L}_Z(\Omega_0)$$

$$- 3\sqrt{\frac{2\pi}{15}}\left(Y_2^{-1} - Y_2^1\right)\Omega_0. \tag{A 5}$$

Further, expanding the orientation probability density as

$$\Omega_0(\boldsymbol{p}) = \sum_{l=0}^{\infty}\sum_{m=-l}^{l} a_{l,m}Y_l^m(\boldsymbol{p}) \tag{A 6}$$

with $a_{l,m}$ being the unknown series coefficients, and substituting in the above equation leads to

$$\nabla_p \cdot (\dot{\boldsymbol{p}}'\Omega_0(\boldsymbol{p})) = \sum_{l=0}^{\infty}\sum_{m=-l}^{l} a_{l,m}\left[\left(\frac{2}{3}\sqrt{\frac{4\pi}{5}}Y_2^0 + \frac{1}{3}\sqrt{4\pi}Y_0^0\right)\mathrm{i}\mathcal{L}_y \mid Y_l^m >\right.$$

$$\left. + \sqrt{\frac{2\pi}{15}}\left(Y_2^{-1} + Y_2^1\right)\mathcal{L}_Z \mid Y_l^m > -3\sqrt{\frac{2\pi}{15}}\left(Y_2^{-1} - Y_2^1\right)Y_l^m\right], \tag{A 7}$$

where $\mathcal{L}_i \mid Y_l^m >= \mathcal{L}_i(Y_l^m)$.

Using (A 6), (A 7) and the following results from Messiah (1962) and Arfken & Weber (1999)

$$i\mathcal{L}_y \mid Y_l^m >= \tfrac{1}{2} \left[\sqrt{l(l+1) - m(m+1)} Y_l^{m+1} - \sqrt{l(l+1) - m(m-1)} Y_l^{m-1} \right], \quad (A\,8)$$

$$\mathcal{L}_z \mid Y_l^m >= m Y_l^m \qquad (A\,9)$$

in (A 1), we have

$$\sum_{l=0}^{\infty} \sum_{m=-l}^{l} a_{l,m} \left\{ \left[Y_l^m - \int d\mathbf{p}' \frac{1}{4\pi} Y_l^m(\mathbf{p}') \right] - D_r \tau \nabla_p^2 Y_l^m + Pe \left[\sqrt{\frac{2\pi}{15}} \left(Y_2^{-1} + Y_2^1 \right) m Y_l^m \right. \right.$$

$$+ \left(\frac{1}{3} \sqrt{\frac{4\pi}{5}} Y_2^0 + \frac{1}{6} \sqrt{4\pi} Y_0^0 \right) \left[\sqrt{l(l+1) - m(m+1)} Y_l^{m+1} \right.$$

$$\left. \left. - \sqrt{l(l+1) - m(m-1)} Y_l^{m-1} \right] - 3\sqrt{\frac{2\pi}{15}} \left(Y_2^{-1} - Y_2^1 \right) Y_l^m \right] \right\} = 0. \qquad (A\,10)$$

Imposing the normalization condition on the base-state probability density

$$\int \Omega_0(\mathbf{p}) \, d\mathbf{p} = 1, \qquad (A\,11)$$

and substituting (A 6) in the above equation, one would get

$$a_{0,0} = 1/\sqrt{4\pi}. \qquad (A\,12)$$

Multiplying (A 10) with a conjugate spherical harmonic $Y_r^{s*}(\mathbf{p})$, using the orthogonality of the spherical harmonics on the unit sphere, and considering $a_{0,0}$ from (A 12), gives the following system of linear equations for the $a_{l,m}$ values:

$$\sum_{l=1}^{\infty} \sum_{m=-l}^{l} a_{l,m} \left\{ [1 + D_r \tau l(l+1)] \delta_{lr} \delta_{ms} + Pe \left[m\sqrt{\frac{2\pi}{15}} \left(\langle r, s | Y_2^{-1} | l, m \rangle + \langle r, s | Y_2^1 | l, m \rangle \right) \right. \right.$$

$$+ \sqrt{l(l+1) - m(m+1)} \left(\frac{1}{3} \sqrt{\frac{4\pi}{5}} \langle r, s | Y_2^0 | l, m+1 \rangle + \frac{\sqrt{4\pi}}{6} \langle r, s | Y_0^0 | l, m+1 \rangle \right)$$

$$- \sqrt{l(l+1) - m(m-1)} \left(\frac{1}{3} \sqrt{\frac{4\pi}{5}} \langle r, s | Y_2^0 | l, m-1 \rangle + \frac{\sqrt{4\pi}}{6} \langle r, s | Y_0^0 | l, m-1 \rangle \right)$$

$$\left. \left. -3\sqrt{\frac{2\pi}{15}} \left(\langle r, s | Y_2^{-1} | l, m \rangle - \langle r, s | Y_2^1 | l, m \rangle \right) \right] \right\}$$

$$= Pe \sqrt{\frac{3}{10}} \left(\langle r, s | Y_2^{-1} | 0, 0 \rangle - \langle r, s | Y_2^1 | 0, 0 \rangle \right), \qquad (A\,13)$$

which may now be solved for the $a_{l,m}$ values with $(l, m) \neq (0, 0)$.

In the above equation

$$\langle a, b|Y_l^m|p, q >\rangle = \int \mathrm{d}\boldsymbol{p} Y_a^{b*}(\boldsymbol{p}) Y_l^m(\boldsymbol{p}) Y_p^q(\boldsymbol{p})$$

$$= (-1)^b \sqrt{\frac{(2a+1)(2l+1)(2p+1)}{4\pi}} \begin{pmatrix} a & l & p \\ 0 & 0 & 0 \end{pmatrix} \begin{pmatrix} a & l & p \\ -b & m & q \end{pmatrix}, \tag{A 14}$$

where the Wigner-3j symbols, $\begin{pmatrix} l1 & l2 & l3 \\ m1 & m2 & m3 \end{pmatrix}$ will be evaluated by using the Racah formula (Messiah 1962; Doi & Edwards 1978; Arfken & Weber 1999). We truncate the infinite system of equations in (A 13) at $l = L_{max}$, and then solve the resulting finite system numerically. The convergence of the results is checked with respect to the number of harmonics retained throughout the work. As expected, at larger Pe, a greater number of harmonics are required for convergence. For the results presented in the main paper, $L_{max} = 10$ was found to be sufficient.

A.2. *Base-state shear stress*

From (2.3), then one may write the shear stress in the base-state as

$$\Sigma_0 = Pe \frac{\partial u_0}{\partial z} - \mathcal{A} \int \mathrm{d}\boldsymbol{p} \Omega_0(\boldsymbol{p}) p_1 p_3, \tag{A 15}$$

where the first term is the solvent viscous stress and the second term is the active stress due to the bacteria. Using $u_0(z) = z$ and the $\Omega_0(\boldsymbol{p})$ expansion (from (A 6)) in the above equation, and employing the orthogonality of spherical harmonics, we get

$$\Sigma_0 = Pe - \mathcal{A}\sqrt{\frac{2\pi}{15}}\left(a_{2,-1} - a_{2,1}\right) = Pe + \Sigma_0^B. \tag{A 16}$$

Here, Σ_0^B is the active stress in the homogeneous state. The base-state being homogeneous, the divergence of this stress is trivially zero.

The threshold activity number for the quiescent instability of bacterial suspension $\mathcal{A}^* = (Cn_0 L^2 U_b \tau) = (30\tau D_r/\mathcal{F}(r))(1 + 1/(6\tau D_r))/(1 - (15\mathcal{G}(r))/C\mathcal{F}(r))(D_r L/U_b)(1 + 1/(6\tau D_r))$ with $\mathcal{F}(r) \approx 1$ for a slender bacterium and $\mathcal{G}(r) \approx 0$ since we are neglecting the passive component of the stress (Subramanian & Koch 2009). The base-state stress variation against shear rate for different $\mathcal{A}$, including the threshold activity number (bacterium with $\tau D_r = 1$, $\mathcal{A}^* \approx 35$) is shown in figure 2(a). The slope of Σ_0^B versus Pe curve in figure 2(a) gives the suspension viscosity (μ_{s0}). From figure 2(a) we can thus see that the suspension viscosity goes to zero Pe_{cr} as discussed in the main text.

Appendix B. Linear stability analysis

Since we are interested in studying gradient banding, spatial variation is retained only in the gradient direction (see figure 8). The resulting non-dimensional equations are

$$\frac{\partial \Omega}{\partial t} + \epsilon \boldsymbol{p} \cdot \nabla_x \Omega - D_r \tau \nabla_p^2 \Omega + Pe\dot\gamma \nabla_p \cdot (\dot{\boldsymbol{p}}'\Omega) + \left[\Omega - \int \mathrm{d}\boldsymbol{p}'' \frac{1}{4\pi}\Omega(\boldsymbol{p}'')\right] = 0, \tag{B 1}$$

and

$$Pe \frac{\partial^2 u}{\partial z^2} = \mathcal{A}\frac{\partial}{\partial z}\int \mathrm{d}\boldsymbol{p} \Omega(z, \boldsymbol{p}) p_1 p_3. \tag{B 2}$$

In (B 1), $\dot{p}' = \dot{p}/\dot{\gamma} = E' \cdot p + \omega' \cdot p - p(E' : pp)$ with $\dot{\gamma} = \partial u/\partial z$, $E' = \frac{1}{2}(\delta_{i1}\delta_{j3} + \delta_{i3}\delta_{j1})$, $\omega' = \frac{1}{2}(\delta_{i1}\delta_{j3} - \delta_{i3}\delta_{j1})$ and δ_{ij} is the Kronecker delta. We consider a small perturbation, with an amplitude $A \ll 1$, of the homogeneously sheared base-state

$$u(z, t) = u_0(z) + Au_1(z, t) + \cdots . \tag{B 3}$$

Correspondingly, the bacterial probability density is expressed as

$$\Omega(p, z, t) = \Omega_0(p) + A\Omega_1(z, p, t) + \cdots . \tag{B 4}$$

Substituting (B 3), (B 4) into (B 1) and (B 2), one has the following equations at $O(A)$:

$$\frac{\partial \Omega_1}{\partial t} + \epsilon p \cdot \nabla_x \Omega_1 - D_r \tau \nabla_p^2 \Omega_1 + Pe \nabla_p \cdot (\dot{p}' \Omega_1) + Pe \dot{\gamma}_1 \nabla_p \cdot (\dot{p}' \Omega_0)$$

$$+ \left[\Omega_1 - \int \mathrm{d}p' \frac{1}{4\pi} \Omega_1(p') \right] = 0 \tag{B 5}$$

and

$$Pe \frac{\partial^2 u_1}{\partial z^2} = \mathcal{A} \frac{\partial}{\partial z} \int \mathrm{d}p \, \Omega_1(z, p) p_1 p_3. \tag{B 6}$$

Here, $\dot{\gamma}_1 = \partial u_1/\partial z$ is the perturbation simple shear flow (the topology of the local perturbation flow remains identical to the base-sate, on account of the assumption of gradient aligned perturbations); (B 5) and (B 6) describe the dynamics at linear order in the perturbation amplitude.

B.1. *Concentration dynamics (CD) – derivation of semi-analytical expression for the growth rate using multiple scale analysis*

In the limit $\epsilon \ll 1$, on account of the separation of time scales between the orientation and spatial degrees of freedom, one may use a multiple scale analysis to analyse the linear stability of the sheared homogeneous state. Accordingly, the time derivative is expanded as

$$\frac{\partial}{\partial t} = \frac{\partial}{\partial t_1} + \epsilon^2 \frac{\partial}{\partial t_2}. \tag{B 7}$$

Expanding the probability density as

$$\Omega_1 = \Omega_{10} + \epsilon \Omega_{11} + \epsilon^2 \Omega_{12} + \cdots, \tag{B 8}$$

and substituting this expansion in (B 5), with the neglect of short time scale of $O(\tau)$ characterizing the orientation dynamics (as represented by $\partial/\partial t_1$), one obtains

$$O(1) : Pe \nabla_p \cdot (\Omega_{10} \dot{p}') + \left[\Omega_{10} - \int \mathrm{d}p' \frac{1}{4\pi} \Omega_{10}(p') \right] - \tau D_r \nabla_p^2 \Omega_{10} = -Pe \dot{\gamma}_1 \nabla_p \cdot (\Omega_0 \dot{p}'), \tag{B 9}$$

$$O(\epsilon) : Pe \nabla_p \cdot (\Omega_{11} \dot{p}') + \left[\Omega_{11} - \int \mathrm{d}p' \frac{1}{4\pi} \Omega_{11}(p') \right] - \tau D_r \nabla_p^2 \Omega_{11} = -p \cdot \nabla_x \Omega_{10}, \tag{B 10}$$

$$O(\epsilon^2) : Pe\nabla_p \cdot (\Omega_{12}\dot{\boldsymbol{p}}') + \left[\Omega_{12} - \int d\boldsymbol{p}' \frac{1}{4\pi}\Omega_{12}(\boldsymbol{p}')\right] - \tau D_r \nabla_p^2 \Omega_{12}$$

$$= -\frac{\partial \Omega_{10}}{\partial t_2} - \boldsymbol{p} \cdot \nabla_x \Omega_{11}. \tag{B 11}$$

Equations (B 9)–(B 11) are complemented by the following normalization conditions:

$$\int d\boldsymbol{p}\,\Omega_{10} = n_1(z, t_2), \tag{B 12}$$

$$\int d\boldsymbol{p}\,\Omega_{11} = \int d\boldsymbol{p}\,\Omega_{12} = 0. \tag{B 13}$$

On account of linearity, we postulate the following form for Ω_{10} to solve (B 9):

$$\Omega_{10} = \Omega_{10}^1 \dot{\gamma}_1(z, t_2) + \Omega_{10}^2 n_1(z, t_2), \tag{B 14}$$

where Ω_{10}^1 is the particular solution that integrates to zero over orientation space, while Ω_{10}^2 is the homogeneous solution that conforms to the aforementioned normalization constraint. Through the active stress in the equations of motion, the perturbation in the probability density function (Ω_1) drives the perturbation shear rate ($\dot{\gamma}_1$). In the following, we derive a reduced relation between them.

Substituting (B 14) in (B 9), (B 12), and equating the $\dot{\gamma}_1$ and n_1 terms, one obtains,

$$\left[\Omega_{10}^1 - \int d\boldsymbol{p}' \frac{1}{4\pi}\Omega_{10}^1(\boldsymbol{p}')\right] - \tau D_r \nabla_p^2 \Omega_{10}^1 + Pe\nabla_p \cdot (\Omega_{10}^1\dot{\boldsymbol{p}}') = -Pe\nabla_p \cdot (\Omega_0\dot{\boldsymbol{p}}'), \tag{B 15}$$

$$\left[\Omega_{10}^2 - \int d\boldsymbol{p}' \frac{1}{4\pi}\Omega_{10}^2(\boldsymbol{p}')\right] - \tau D_r \nabla_p^2 \Omega_{10}^2 + Pe\nabla_p \cdot (\Omega_{10}^2\dot{\boldsymbol{p}}') = 0, \tag{B 16}$$

with the respective integral constraints being,

$$\int d\boldsymbol{p}\,\Omega_{10}^1 = 0, \tag{B 17}$$

and

$$\int d\boldsymbol{p}\,\Omega_{10}^2 = 1. \tag{B 18}$$

The unknown component probability densities Ω_{10}^1 and Ω_{10}^2 in (B 15)–(B 18) are again be determined from an expansion in spherical harmonics. Thus writing

$$\Omega_{10}^1 = \sum_{l=0}^{\infty} \sum_{m=-l}^{m=l} c_{l,m} Y_l^m, \tag{B 19}$$

$$\Omega_{10}^2 = \sum_{l=0}^{\infty} \sum_{m=-l}^{m=l} d_{l,m} Y_l^m, \tag{B 20}$$

the unknown coefficients $c_{l,m}$ and $d_{l,m}$ in the resulting equations are obtained by employing the numerical scheme similar to the one mentioned in appendix A while evaluating $\Omega_0(\boldsymbol{p})$.

Substituting Ω_{10} from (B 14) in the right-hand side of (B 10), we have

$$\left[\Omega_{11} - \int \mathrm{d}\boldsymbol{p}' \frac{1}{4\pi} \Omega_{11}(\boldsymbol{p}')\right] - \tau D_r \nabla_p^2 \Omega_{11} + Pe \nabla_p \cdot (\Omega_{11}\dot{\boldsymbol{p}}) = -\boldsymbol{p} \cdot \nabla_x \Omega_{10}$$

$$= -\cos\theta \sum_{l'=0}^{\infty} \sum_{m'=-l'}^{l'} \left[c_{l',m'} \frac{\partial \dot{\gamma}_1}{\partial z} + d_{l',m'} \frac{\partial n_1}{\partial z} \right] Y_{l'}^{m'}(\boldsymbol{p}). \quad \text{(B 21)}$$

Again, on account of linearity, one may write

$$\Omega_{11} = \Omega_{11}^1 \frac{\partial \dot{\gamma}_1}{\partial z} + \Omega_{11}^2 \frac{\partial n_1}{\partial z}, \quad \text{(B 22)}$$

and substituting in (B 13), (B 21), and equating the coefficients of $\partial \dot{\gamma}_1/\partial z$ and $\partial n_1/\partial z$, we get

$$\left[\Omega_{11}^1 - \int \mathrm{d}\boldsymbol{p}' \frac{1}{4\pi} \Omega_{11}^1(\boldsymbol{p}')\right] - \tau D_r \nabla_p^2 \Omega_{11}^1 + Pe \nabla_p \cdot (\Omega_{11}^1 \dot{\boldsymbol{p}})$$

$$= -\cos\theta \sum_{l'=0}^{\infty} \sum_{m'=-l'}^{l'} c_{l',m'} Y_{l'}^{m'}, \quad \text{(B 23)}$$

$$\left[\Omega_{11}^2 - \int \mathrm{d}\boldsymbol{p}' \frac{1}{4\pi} \Omega_{11}^2(\boldsymbol{p}')\right] - \tau D_r \nabla_p^2 \Omega_{11}^2 + Pe \nabla_p \cdot (\Omega_{11}^2 \dot{\boldsymbol{p}})$$

$$= -\cos\theta \sum_{l'=0}^{\infty} \sum_{m'=-l'}^{l'} d_{l',m'} Y_{l'}^{m'}, \quad \text{(B 24)}$$

with trivial normalization constraints given by

$$\int \Omega_{11}^1 \, \mathrm{d}\boldsymbol{p} = \int \Omega_{11}^2 \, \mathrm{d}\boldsymbol{p} = 0. \quad \text{(B 25)}$$

The probability densities Ω_{11}^1, Ω_{11}^2 can again be expanded as $\Omega_{11}^1 = \sum_{l=0}^{\infty} \sum_{m=-l}^{m=l} e_{l,m} Y_l^m$, $\Omega_{11}^2 = \sum_{l=0}^{\infty} \sum_{m=-l}^{m=l} f_{l,m} Y_l^m$. Substitution in (B 23)–(B 25) allows one to solve for the unknown coefficients $e_{l,m}, f_{l,m}$ obtained by employing the numerical scheme above.

Using (B 17), (B 18) and (B 22) in (B 11) and integrating over the orientation degrees of freedom, one obtains the following drift-diffusivity equation (Nitsche & Hinch 1997; Subramanian & Brady 2004; Kasyap & Koch 2012, 2014) at $O(A)$:

$$\frac{\partial n_1}{\partial t_2} = \frac{\partial}{\partial z}\left(-V_1(z).1 + D_0 \frac{\partial n_1}{\partial z}\right) \quad \text{(B 26)}$$

in position space alone. Here, $V_1 = 2\sqrt{\pi/3} e_{1,0}(\partial \dot{\gamma}_1/\partial z)$ is the destabilizing drift that multiplies the base-state number density (1 in non-dimensional terms) and $D_0 = -2\sqrt{\pi/3} f_{1,0}$ is the stabilizing diffusivity. (B 26) is given as (3.2) in § 3.1.

The variation in the perturbation shear rate is driven by the probability density variation, and hence the perturbation stress, through the equations of motion.

Substituting $\Omega_1 = \Omega_{10} + \epsilon \Omega_{11} + \epsilon^2 \Omega_{12} + \cdots$, using (B 14) and (B 20) in (B 6) and equating the leading-order terms on both sides,

$$Pe \frac{\partial^2 u_1(z, t_2)}{\partial z^2} = \mathcal{A} \frac{\partial}{\partial z} \int \mathrm{d}\boldsymbol{p} \left[\sum_{l=0}^{\infty} \sum_{m=-l}^{l} \left(\dot{\gamma}_1(z, t_2) c_{l,m} + n_1(z, t_2) d_{l,m} \right) Y_l^m(\boldsymbol{p}) \right]$$

$$\times \sqrt{\frac{2\pi}{15}} (Y_2^{-1}(\boldsymbol{p}) - Y_2^1(\boldsymbol{p})), \tag{B 27}$$

$$\Rightarrow \frac{\partial \dot{\gamma}_1(z, t_2)}{\partial z} \left[Pe - \mathcal{A} \sqrt{\frac{2\pi}{15}} \left(c_{2,-1} - c_{2,1} \right) \right] = \mathcal{A} \sqrt{\frac{2\pi}{15}} \left(d_{2,-1} - d_{2,1} \right) \frac{\partial n_1(z, t_2)}{\partial z}. \tag{B 28}$$

Using the normal mode forms $n_1(z, t_2) = \tilde{n}_1 \cos(zk_z) \exp(\sigma t_2)$, $\dot{\gamma}_1(z, t_2) = \tilde{\dot{\gamma}}_1 \cos(zk_z)$ $\exp(\sigma t_2)$ in the above equation, and from (A 1), (B 16), (A 16), we get

$$\tilde{\dot{\gamma}}_1 = \tilde{n}_1 \frac{\sqrt{\dfrac{2\pi}{15}} \mathcal{A}(d_{2,-1} - d_{2,1})}{\left[Pe - \sqrt{\dfrac{2\pi}{15}} \mathcal{A}(c_{2,-1} - c_{2,1}) \right]} = \tilde{n}_1 \frac{|\Sigma_0^B|}{\left[Pe - \sqrt{\dfrac{2\pi}{15}} \mathcal{A}(c_{2,-1} - c_{2,1}) \right]}. \tag{B 29}$$

Substituting $\dot{\gamma}_1$ and n_1 in (B 26), using (B 29), one would get the growth rate expression as

$$\sigma = k_z^2 \left(2\sqrt{\frac{\pi}{3}} e_{1,0} \frac{|\Sigma_0^B|}{Pe\mu_{s0}} - D_0 \right), \tag{B 30}$$

where, $\mu_{s0} = 1 - (\mathcal{A}/Pe)\sqrt{2\pi/15}(c_{2,-1} - c_{2,1})$ is the viscosity of the homogeneously sheared state. The expression for growth rate, give by (B 30), appears as (3.5) in § 3.1.

B.2. *Coupled concentration–orientation dynamics (CCOD) – numerical solution for the growth rate*

In this section we describe the numerical formulation for the full linear stability analysis without any assumption with regard to a time scale separation. As before, introducing a layering perturbation, and an amplitude $A \ll 1$, to the base-state simple shear, of the form

$$u(z, t) = u_0(z) + A u_1(z, t) + \cdots, \tag{B 31}$$

with the corresponding perturbations to the probability density and shear rate being

$$\Omega = \Omega_0(\boldsymbol{p}) + A\Omega_1(\boldsymbol{p}, z, t) + \cdots, \tag{B 32}$$

$$\dot{\gamma}(z, t) = \frac{\partial u}{\partial z} = \dot{\gamma}_0 + A\dot{\gamma}_1(z, t) + \cdots, \tag{B 33}$$

substituting (B 32) and (B 33) in (2.1) and collecting terms at successive orders, one obtains

$$O(1) : \dot{\gamma}_0 \nabla_p(\dot{\boldsymbol{p}}'\Omega_0) - D_r \nabla_p^2 \Omega_0 + \frac{1}{\tau} \left[\Omega_0 - \int \mathrm{d}\boldsymbol{p}' \frac{1}{4\pi} \Omega_0(\boldsymbol{p}') \right] = 0, \tag{B 34}$$

$$O(A): \frac{\partial \Omega_1}{\partial t} + U_b \boldsymbol{p} \cdot \nabla_x \Omega_1 - D_r \nabla_p^2 \Omega_1 + \dot{\gamma}_0 \nabla_p (\dot{\boldsymbol{p}}' \Omega_1) + \dot{\gamma}_1 \nabla_p (\dot{\boldsymbol{p}}' \Omega_0)$$

$$+ \frac{1}{\tau} \left[\Omega_1 - \int d\boldsymbol{p}' \frac{1}{4\pi} \Omega_1(\boldsymbol{p}') \right] = 0. \tag{B 35}$$

Using τ, $U_b \tau$ (as opposed to H in the multiple scale analysis earlier), U_b are the scales for time, length, velocity, (B 34) and (B 35) in dimensionless form are given by,

$$O(1): Pe \nabla_p (\dot{\boldsymbol{p}}' \Omega_0) - \tau D_r \nabla_p^2 \Omega_0 + \left[\Omega_0 - \int d\boldsymbol{p}' \frac{1}{4\pi} \Omega_0(\boldsymbol{p}') \right] = 0, \tag{B 36}$$

$$O(A): \frac{\partial \Omega_1}{\partial t} + \boldsymbol{p} \cdot \nabla_x \Omega_1 - \tau D_r \nabla_p^2 \Omega_1 + Pe \nabla_p (\dot{\boldsymbol{p}}' \Omega_1) + \dot{\gamma}_1 \nabla_p (\dot{\boldsymbol{p}}' \Omega_0)$$

$$+ \left[\Omega_1 - \int d\boldsymbol{p}' \frac{1}{4\pi} \Omega_1(\boldsymbol{p}') \right] = 0, \tag{B 37}$$

where $Pe = \dot{\gamma}_0 \tau$. Assuming the usual normal mode form

$$\Omega_1(z, \boldsymbol{p}, t) = \tilde{\Omega}_1(k_z, \boldsymbol{p}) \exp(izk_z + \sigma t) \tag{B 38}$$

and

$$u_1(z, t) = \tilde{u}_1(k_z) \exp(izk_z + \sigma t) \tag{B 39}$$

and substituting in (B 37), one obtains

$$\tilde{\Omega}_1 \sigma + (ik_z \cos\theta) \tilde{\Omega}_1 + Pe \nabla_p \cdot (\dot{\boldsymbol{p}}' \tilde{\Omega}_1) + ik_z \tilde{u}_1 \nabla_p \cdot (\dot{\boldsymbol{p}}' \tilde{\Omega}_0) - \tau D_r \nabla_p^2 \tilde{\Omega}_1$$

$$+ \left[\tilde{\Omega}_1 - \int d\boldsymbol{p}' \frac{1}{4\pi} \tilde{\Omega}_1(\boldsymbol{p}') \right] = 0. \tag{B 40}$$

Substituting (B 31), (B 32) in (2.3), the momentum equation, at $O(A)$, takes the form,

$$\frac{\partial^2 u_1}{\partial z^2} = A \frac{\partial}{\partial z} \int d\boldsymbol{p} \Omega_1(z, \boldsymbol{p}) p_1 p_3. \tag{B 41}$$

Using, (B 38) and (B 39) in the above equation, one has the following relation coupling the perturbation shear to the probability density:

$$\tilde{u}_1 = -\frac{iA}{k_z} \int d\boldsymbol{p} \tilde{\Omega}_1(k_z, \boldsymbol{p}) p_1 p_3. \tag{B 42}$$

Using $\tilde{u}_1$ from (B 42) in (B 40), one obtains

$$Pe \nabla_p \cdot (\dot{\boldsymbol{p}}' \tilde{\Omega}_1) + (ik_z \cos\theta) \tilde{\Omega}_1 + A \left(\int d\boldsymbol{p} \tilde{\Omega}_1(k_z, \boldsymbol{p}) p_1 p_3 \right) \nabla_p \cdot (\dot{\boldsymbol{p}}' \Omega_0)$$

$$- \tau D_r \nabla_p^2 \tilde{\Omega}_1 + \left[\tilde{\Omega}_1 - \int d\boldsymbol{p}' \frac{1}{4\pi} \tilde{\Omega}_1(\boldsymbol{p}') \right] = -\tilde{\Omega}_1 \sigma. \tag{B 43}$$

The unknown Ω_0 in the above equation is obtained numerically, as already explained, in terms of a spherical harmonic series (see appendix A). Substituting the known from for

Ω_0 and expanding $\tilde{\Omega}_1$ as

$$\tilde{\Omega}_1 = \sum_{l=0}^{N} \sum_{m=-l}^{l} b_{l,m} Y_l^m(\boldsymbol{p}) \tag{B 44}$$

in terms of spherical harmonics, and following the numerical procedure in appendix A.1, we solve the resulting eigenvalue problem.

The method yields the entire eigenspectrum, but we focus on the unstable eigenvalue which gives the growth rate. The variation in the leading growth rate value of coupled concentration–orientation dynamics (real(σ)) and the growth rate of concentration dynamics against *Pe* has been compared in figure 3 in the main text.

B.3. *Number density perturbations*

The normalization condition of the bacterial probability density ((B 8), (B 12) and (B 13)) gives

$$\int \mathrm{d}\boldsymbol{p}\,\Omega_1 = n_1. \tag{B 45}$$

Substituting Ω_1 from (B 38) and using $n_1 = \tilde{n}_1 \exp(\mathrm{i}zk_z + \sigma t)$ in the above equation, one obtains

$$\int \mathrm{d}\boldsymbol{p}\,\tilde{\Omega}_1 = \tilde{n}_1. \tag{B 46}$$

Now substituting $\tilde{\Omega}_1$ expansion from (B 44) in the above equation and after simplification, we obtain the number density perturbation amplitude $\tilde{n}_1 = \sqrt{4\pi}\,b_{0,0}$. The leading growth rate value (real(σ)), and the corresponding number density perturbation against wavenumber for different *Pe* have been plotted in figure 4.

Appendix C. Nonlinear simulations

For the nonlinear simulations, the bacterial orientations are assumed to be confined to the shear-gradient plane, so in contrast to that shown in figure 8, $\boldsymbol{p}$ in the simulations is taken as $\cos\theta \mathbf{1}_x + \sin\theta \mathbf{1}_z$. The Stokes equations are used to express the shear rate variation along the gradient direction in terms of Ω, so that the kinetic equation takes the form of a nonlinear integro-differential equation for Ω. Then, the orientation and spatial dependence of the unknown variable, Ω, is expanded in a Fourier series as follows:

$$\Omega = \sum_{m=-N_p}^{N_p} \sum_{k=-N_k}^{N_k} a_m^k \exp(\mathrm{i}kz + \mathrm{i}m\theta). \tag{C 1}$$

A standard Galerkin projection gives a set of coupled ordinary differential equations for the a_m^k values, which are integrated in time using a second-order Runge–Kutta scheme (Boyd 2001; Canuto *et al.* 2012). Convergence is checked with respect to both N_p and N_k and it is found that 17 orientation harmonics and 301 spatial harmonics are sufficient for convergence for all the results presented in the paper. The steady state can consist of multiple bands depending on the particular initial condition, as is known from earlier work on passive complex fluids (Fielding & Olmsted 2003). Thus, a suitable initial condition is
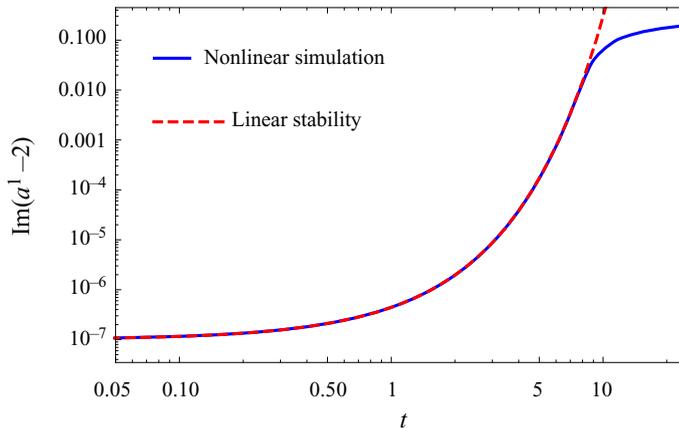
FIGURE 9. Comparison of the time evolution of a^1_{-2} obtained independently from the nonlinear simulation and linear stability approaches.

chosen for which the minimum number of bands are present in the steady state. For the results shown in § 3.3, the following initial condition was chosen, for every k, for $m > 0$

$$a^k_m(0) = 0.0000001 + 0.0000001i, \tag{C 2}$$

for $m < 0$

$$a^k_m(0) = 0.0000001 - 0.0000001i, \tag{C 3}$$

and $a^k_0(0) = 0.0000001$.

In order to verify the simulation results, we carried out a linear stability analysis where the orientation vector is also restricted to the flow-gradient plane. The linear stability analysis predicts for each term a^k_m,

$$a^k_m(t) = a^k_m(0)\,\mathrm{e}^{\sigma t}, \tag{C 4}$$

where σ is the eigenvalue to be numerically obtained. Figure 9 shows that the results obtained using the two different methods are in agreement.

REFERENCES

ARFKEN, G. B. & WEBER, H. J. 1999 *Mathematical Methods for Physicists*. Academic Press.

BARRY, M. T., RUSCONI, R., GUASTO, J. S. & STOCKER, R. 2015 Shear-induced orientational dynamics and spatial heterogeneity in suspensions of motile phytoplankton. *J. R. Soc. Interface* **12** (112), 20150791.

BATCHELOR, G. K. 1970 The stress system in a suspension of force-free particles. *J. Fluid Mech.* **41** (3), 545–570.

BEARON, R. N. & HAZEL, A. L. 2015 The trapping in high-shear regions of slender bacteria undergoing chemotaxis in a channel. *J. Fluid Mech.* **771**, R3.

BECHTEL, T. M. & KHAIR, A. S. 2017 Linear viscoelasticity of a dilute active suspension. *Rheol. Acta* **56** (2), 149–160.

BERKE, A. P., TURNER, L., BERG, H. C. & LAUGA, E. 2008 Hydrodynamic attraction of swimming microorganisms by surfaces. *Phys. Rev. Lett.* **101** (3), 038102.

BOYD, J. P. 2001 *Chebyshev and Fourier Spectral Methods*. Courier Corporation.

CANUTO, C., HUSSAINI, M. Y., QUARTERONI, A. & THOMAS, A. JR 2012 *Spectral Methods in Fluid Dynamics*. Springer Science and Business Media.

CATES, M. E. & FIELDING, S. M. 2006 Rheology of giant micelles. *Adv. Phys.* **55** (7–8), 799–879.

CATES, M. E., FIELDING, S. M., MARENDUZZO, D., ORLANDINI, E. & YEOMANS, J. M. 2008 Shearing active gels close to the isotropic-nematic transition. *Phys. Rev. Lett.* **101** (6), 068102.

CLEMENT, E., LINDNER, A., DOUARCHE, C. & AURADOU, H. 2016 Bacterial suspensions under flow. *Eur. Phys. J.* **225** (11–12), 2389–2406.

CROMER, M., FREDRICKSON, G. H. & LEAL, L. G. 2014 A study of shear banding in polymer solutions. *Phys. Fluids* **26** (6), 063101.

CROMER, M., VILLET, M. C., FREDRICKSON, G. H. & LEAL, L. G. 2013 Shear banding in polymer solutions. *Phys. Fluids* **25** (5), 051703.

DE GENNES, P.-G. & PROST, J. 1993 *The Physics of Liquid Crystals*, vol. 83. Oxford University Press.

DHONT, J. K. G. & BRIELS, W. J. 2008 Gradient and vorticity banding. *Rheol. Acta* **47** (3), 257–281.

DIVOUX, T., FARDIN, M. A., MANNEVILLE, S. & LEROUGE, S. 2016 Shear banding of complex fluids. *Annu. Rev. Fluid Mech.* **48**, 81–103.

DIXON, P. K., PINE, D. J. & WU, X.-L. 1992 Mode selection in the dynamics of sheared polymer solutions. *Phys. Rev. Lett.* **68** (14), 2239.

DOI, M. & EDWARDS, S. F. 1978 Dynamics of rod-like macromolecules in concentrated solution. Part 2. *J. Chem. Soc. Faraday Trans.* **74**, 918–932.

DOMBROWSKI, C., CISNEROS, L., CHATKAEW, S., GOLDSTEIN, R. E. & KESSLER, J. O. 2004 Self-concentration and large-scale coherence in bacterial dynamics. *Phys. Rev. Lett.* **93** (9), 098103.

DOOSTMOHAMMADI, A., IGNÉS-MULLOL, J., YEOMANS, J. M. & SAGUÉS, F. 2018 Active nematics. *Nat. Commun.* **9** (1), 1–13.

DRESCHER, K., DUNKEL, J., CISNEROS, L. H., GANGULY, S. & GOLDSTEIN, R. E. 2011 Fluid dynamics and noise in bacterial cell–cell and cell–surface scattering. *Proc. Natl Acad. Sci. USA* **108** (27), 10940–10945.

DUNKEL, J., HEIDENREICH, S., DRESCHER, K., WENSINK, H. H., BÄR, M. & GOLDSTEIN, R. E. 2013 Fluid dynamics of bacterial turbulence. *Phys. Rev. Lett.* **110** (22), 228102.

ELGETI, J. & GOMPPER, G. 2016 Microswimmers near surfaces. *Eur. Phys. J.* **225** (11–12), 2333–2352.

EZHILAN, B. & SAINTILLAN, D. 2015 Transport of a dilute active suspension in pressure-driven channel flow. *J. Fluid Mech.* **777**, 482–522.

FIELDING, S. M. 2005 Linear instability of planar shear banded flow. *Phys. Rev. Lett.* **95** (13), 134501.

FIELDING, S. M., MARENDUZZO, D. & CATES, M. E. 2011 Nonlinear dynamics and rheology of active fluids: simulations in two dimensions. *Phys. Rev.* E **83** (4), 041910.

FIELDING, S. M. & OLMSTED, P. D. 2003 Flow phase diagrams for concentration-coupled shear banding. *Eur. Phys. J.* E **11** (1), 65–83.

GACHELIN, J., MINO, G., BERTHET, H., LINDNER, A., ROUSSELET, A. & CLÉMENT, É. 2013 Non-newtonian viscosity of escherichia coli suspensions. *Phys. Rev. Lett.* **110** (26), 268103.

GACHELIN, J., ROUSSELET, A., LINDNER, A. & CLEMENT, E. 2014 Collective motion in an active suspension of escherichia coli bacteria. *New. J. Phys.* **16** (2), 025003.

GIOMI, L., LIVERPOOL, T. B. & MARCHETTI, M. C. 2010 Sheared active fluids: thickening, thinning, and vanishing viscosity. *Phys. Rev.* E **81** (5), 051908.

GIOMI, L., MARCHETTI, M. C. & LIVERPOOL, T. B. 2008 Complex spontaneous flows and concentration banding in active polar films. *Phys. Rev. Lett.* **101** (19), 198101.

GUO, S., SAMANTA, D., PENG, Y., XU, X. & CHENG, X. 2018 Symmetric shear banding and swarming vortices in bacterial superfluids. *Proc. Natl Acad. Sci.* **115** (28), 7212–7217.

HATWALNE, Y., RAMASWAMY, S., RAO, M. & SIMHA, R. A. 2004 Rheology of active-particle suspensions. *Phys. Rev. Lett.* **92** (11), 118101.

HELFAND, E. & FREDRICKSON, G. H. 1989 Large fluctuations in polymer solutions under shear. *Phys. Rev. Lett.* **62** (21), 2468.

JEFFERY, G. B. 1922 The motion of ellipsoidal particles immersed in a viscous fluid. *Proc. R. Soc. Lond.* A **102**, 161.

KASYAP, T. V. & KOCH, D. L. 2012 Chemotaxis driven instability of a confined bacterial suspension. *Phys. Rev. Lett.* **108** (3), 038101.

KASYAP, T. V. & KOCH, D. L. 2014 Instability of an inhomogeneous bacterial suspension subjected to a chemo-attractant gradient. *J. Fluid Mech.* **741**, 619–657.

KASYAP, T. V., KOCH, D. L. & WU, M. 2014 Bacterial collective motion near the contact line of an evaporating sessile drop. *Phys. Fluids* **26** (11), 111703.

KOCH, D. L. & SUBRAMANIAN, G. 2011 Collective hydrodynamics of swimming microorganisms: living fluids. *Annu. Rev. Fluid Mech.* **43**, 637–659.

KRISHNAMURTHY, D. & SUBRAMANIAN, G. 2015 Collective motion in a suspension of micro-swimmers that run-and-tumble and rotary diffuse. *J. Fluid Mech.* **781**, 422–466.

LARSON, R. G. 1992 Flow-induced mixing, demixing, and phase transitions in polymeric fluids. *Rheol. Acta* **31** (6), 497–520.

LARSON, R. G. 2013 *Constitutive Equations for Polymer Melts and Solutions: Butterworths Series in Chemical Engineering.* Butterworth-Heinemann.

LI, H., SHI, X.-Q., HUANG, M., CHEN, X., XIAO, M., LIU, C., CHATÉ, H. & ZHANG, H. P. 2019 Data-driven quantitative modeling of bacterial active nematics. *Proc. Natl Acad. Sci.* **116** (3), 777–785.

LOISY, A., EGGERS, J. & LIVERPOOL, T. B. 2018 Active suspensions have nonmonotonic flow curves and multiple mechanical equilibria. *Phys. Rev. Lett.* **121**, 018001.

LÓPEZ, H. M., GACHELIN, J., DOUARCHE, C., AURADOU, H. & CLÉMENT, E. 2015 Turning bacteria suspensions into superfluids. *Phys. Rev. Lett.* **115**, 028301.

MACKAPLOW, M. B. & SHAQFEH, E. S. G. 1998 A numerical study of the sedimentation of fibre suspensions. *J. Fluid Mech.* **376**, 149–182.

MARCHETTI, M. C., JOANNY, J. -F., RAMASWAMY, S., LIVERPOOL, T. B., PROST, J., RAO, M. & SIMHA, R. A. 2013 Hydrodynamics of soft active matter. *Rev. Mod. Phys.* **85** (3), 1143.

MARTINEZ, V. A., CLÉMENT, E., ARLT, J., DOUARCHE, C., DAWSON, A., SCHWARZ-LINEK, J., CREPPY, A. K., ŠKULTÉTY, V., MOROZOV, A. N. Auradou, H. *et al.* 2020 A combined rheometry and imaging study of viscosity reduction in bacterial suspensions. *Proc. Natl Acad. Sci.* **117** (5), 2326–2331.

MESSIAH, A. 1962 Quantum Mechanics, vol. 2. North-Holland.

MILES, C. J., EVANS, A. A., SHELLEY, M. J. & SPAGNOLIE, S. E. 2019 Active matter invasion of a viscous fluid: unstable sheets and a no-flow theorem. *Phys. Rev. Lett.* **122** (9), 098002.

MILNER, S. T. 1993 Dynamical theory of concentration fluctuations in polymer solutions under shear. *Phys. Rev.* E **48** (5), 3674.

NAMBIAR, S., GARG, P. & SUBRAMANIAN, G. 2019*a* Enhanced velocity fluctuations in interacting swimmer suspensions. arXiv:1902.05304.

NAMBIAR, S., NOTT, P. R. & SUBRAMANIAN, G. 2017 Stress relaxation in a dilute bacterial suspension. *J. Fluid Mech.* **812**, 41–64.

NAMBIAR, S., PHANIKANTH, S., NOTT, P. R. & SUBRAMANIAN, G. 2019*b* Stress relaxation in a dilute bacterial suspension: the active–passive transition. *J. Fluid Mech.* **870**, 1072–1104.

NITSCHE, L. C. & HINCH, E. J. 1997 Shear-induced lateral migration of brownian rigid rods in parabolic channel flow. *J. Fluid Mech.* **332**, 1–21.

OLMSTED, P. D. 2008 Perspectives on shear banding in complex fluids. *Rheol. Acta* **47** (3), 283–300.

ONUKI, A. 2002 *Phase Transition Dynamics.* Cambridge University Press.

PAHLAVAN, A. A. & SAINTILLAN, D. 2011 Instability regimes in flowing suspensions of swimming micro-organisms. *Phys. Fluids* **23** (1), 011901.

RUSCONI, R., GUASTO, J. S. & STOCKER, R. 2014 Bacterial transport suppressed by fluid shear. *Nat. Phys.* **10** (3), 212.

SAINTILLAN, D. 2010 The dilute rheology of swimming suspensions: a simple kinetic model. *Exp. Mech.* **50** (9), 1275–1281.

SAINTILLAN, D. 2018 Rheology of active fluids. *Annu. Rev. Fluid Mech.* **50**, 563–592.

SAINTILLAN, D. & SHELLEY, M. J. 2007 Orientational order and instabilities in suspensions of self-locomoting rods. *Phys. Rev. Lett.* **99** (5), 058102.

SAINTILLAN, D. & SHELLEY, M. J. 2008*a* Instabilities and pattern formation in active particle suspensions: kinetic theory and continuum simulations. *Phys. Rev. Lett.* **100** (17), 178103.

SAINTILLAN, D. & SHELLEY, M. J. 2008*b* Instabilities, pattern formation, and mixing in active suspensions. *Phys. Fluids* **20** (12), 123304.

A7-30   *L. Vennamneni, P. Garg and G. Subramanian*

SANCHEZ, T., CHEN, D. T. N., DECAMP, S. J., HEYMANN, M. & DOGIC, Z. 2012 Spontaneous motion in hierarchically assembled active matter. *Nature* **491** (7424), 431–434.

SCHWARZ-LINEK, J., ARLT, J., JEPSON, A., DAWSON, A., VISSERS, T., MIROLI, D., PILIZOTA, T., MARTINEZ, V. A. & POON, W. C. K. 2016 Escherichia coli as a model active colloid: a practical introduction. *Colloids Surf.* B **137**, 2–16.

SECCHI, E., RUSCONI, R., BUZZACCARO, S., SALEK, M. M., SMRIGA, S., PIAZZA, R. & STOCKER, R. 2016 Intermittent turbulence in flowing bacterial suspensions. *J. R. Soc. Interface* **13** (119), 20160175.

SIMHA, R. A. & RAMASWAMY, S. 2002 Hydrodynamic fluctuations and instabilities in ordered suspensions of self-propelled particles. *Phys. Rev. Lett.* **89** (5), 058101.

SOKOLOV, A. & ARANSON, I. S. 2009 Reduction of viscosity in suspension of swimming bacteria. *Phys. Rev. Lett.* **103** (14), 148101.

SOKOLOV, A. & ARANSON, I. S. 2012 Physical properties of collective motion in suspensions of bacteria. *Phys. Rev. Lett.* **109** (24), 248109.

SOKOLOV, A. & ARANSON, I. S. 2016 Rapid expulsion of microswimmers by a vortical flow. *Nat. Commun.* **7**, 11114.

SOKOLOV, A., ARANSON, I. S., KESSLER, J. O. & GOLDSTEIN, R. E. 2007 Concentration dependence of the collective dynamics of swimming bacteria. *Phys. Rev. Lett.* **98** (15), 158102.

STENHAMMAR, J., NARDINI, C., NASH, R. W., MARENDUZZO, D. & MOROZOV, A. 2017 Role of correlations in the collective behavior of microswimmer suspensions. *Phys. Rev. Lett.* **119** (2), 028005.

SUBRAMANIAN, G. & BRADY, J. F. 2004 Multiple scales analysis of the Fokker–Planck equation for simple shear flow. *Physica* A **334** (3–4), 343–384.

SUBRAMANIAN, G. & KOCH, D. L. 2009 Critical bacterial concentration for the onset of collective swimming. *J. Fluid Mech.* **632**, 359–400.

UNDERHILL, P. T., HERNANDEZ-ORTIZ, J. P. & GRAHAM, M. D. 2008 Diffusion and spatial correlations in suspensions of swimming particles. *Phys. Rev. Lett.* **100** (24), 248101.

VENNAMNENI, L., NAMBIAR, S. & SUBRAMANIAN, G. 2020 Shear-induced migration of microswimmers in pressure-driven channel flow. *J. Fluid Mech.* **890**, A15.

WENSINK, H. H., DUNKEL, J., HEIDENREICH, S., DRESCHER, K., GOLDSTEIN, R. E., LÖWEN, H. & YEOMANS, J. M. 2012 Meso-scale turbulence in living fluids. *Proc. Natl Acad. Sci. USA* **109** (36), 14308–14313.

WU, X.-L. & LIBCHABER, A. 2000 Particle diffusion in a quasi-two-dimensional bacterial bath. *Phys. Rev. Lett.* **84** (13), 3017.

WU, X.-L., PINE, D. J. & DIXON, P. K. 1991 Enhanced concentration fluctuations in polymer solutions under shear flow. *Phys. Rev. Lett.* **66** (18), 2408.